ISSN: 1757-899X

Materials Science and Engineering

Volume No. 11
Issue No. 2
May - August 2025

ENRICHED PUBLICATIONS

Enriched Publications
S-9,IInd FLOOR, MLU POCKET,
MANISH ABHINAV PLAZA-II, ABOVE FEDERAL BANK,
PLOT NO-5, SECTOR -5, DWARKA, NEW DELHI, INDIA-110075,
PHONE: - + (91)-(11)-45525005

ISSN: 1757-899X

Materials Science and Engineering

Aims and Scope

IOP Conference Series: Materials Science and Engineering (MSE) is an Open Access proceedings journal provides a fast, versatile and cost-effective proceedings publication service.

Subjects

- Processing, Manufacturing and applications
- Analysis and characterisation
- Functional materials
- Polymer science
- Glasses and ceramics
- Thin films and surfaces
- Nanostructures and nanomaterials
- Composites
- Biomaterials
- Environment and energy
- Computation and simulation
- Crystalline structure and microstructure
- Structural and mechanical
- Measurement and systems
- Metals, alloys and metallurgy
- Engineering (Electrical, Mechanical, Civil, Chemical and Neuromorphic Computing)

ISSN: 1757-899X

Materials Science and Engineering

Managing Editor
Mr. Amit Prasad

ISSN: 1757-899X

Materials Science and Engineering

(Volume No. 11, Issue No. 2, May - Aug 2025)

Contents

Sr. No.	Articles / Authors Name	Pg. No.
1	Characterization of the milling-induced hardness gradient in the near-surface material volume of high manganese TWIP steel 1.7401 by nanoindentation - *S. Wolke * , M. Smaga, T. Beck*	1 - 33
2	From a notch to a crack: Monitoring crack initiation from a notch through cyclic bending of microscale cantilevers - *Ali Kaveh 1, M.H. Shahini1, Xiaoman Zhang 1 , Wangwang Xu, Parisa Z. Firouzabadi, Bin Zhang, W.J. Meng **	34 - 55

ISSN: 1757-899X

Characterization of the milling-induced hardness gradient in the near-surface material volume of high manganese TWIP steel 1.7401 by nanoindentation

S. Wolke * , M. Smaga, T. Beck
Institute of Materials Science and Engineering, University of Kaiserslautern-Landau, Germany

ABSTRACT

The hardness gradient induced by up and down milling in the near-surface material volume of high-manganese TWIP steel 1.7401 was characterised up to a surface distance of 50 μ m using nanoindentation. Hereby, even the influence of various small indentation depths was such pronounced that the indentation size effect influenced the measured hardness significantly and was, hence, studied. In a first step, the effect of uniaxial, quasi-static deformation on hardness was investigated, which serves as a comparison to hardening by milling which is associated with a complex, multiaxial deformation. Subsequently, suitable parameters for characterization of the milling induced hardness gradient were identified through variation of indentation depths and indentation depth-to-indent spacing ratios. Additionally, the near-surface hardness gradient was examined transversely and longitudinally to the feed direction to analyse whether possible process-induced differences occur due to intermittent cutting. Furthermore, the hardness in the nanocrystalline layer was examined in detail and correlated with the respective microstructures, observed through FIB cutting and ion beam imaging. Finally, the hardness gradients after up and down milling were compared, the effect of electrolytic polishing on the near surface hardness gradient was analysed and the hardness in the rolling skin, representing the initial state, was studied. Milling results in a maximum increase in hardness of approximately 50 % in comparison with the base material, and the hardness decreases degressively with increasing distance to the surface up to a depth of approximately 20 μ m. Hardness increases in the milling-induced near-surface material which can be attributed to higher dislocation density. The near-surface layer, measuring 1–2 μ m in depth, consists of fine-grained material, and the transition to coarser grains corresponds with a change in hardness slope. No significant hardness gradient was detected along the feed direction, and up and down milling results in similar hardness gradients.

Keywords: Nanoindentation Indentation size effect Continuous stiffness measurement Surface hardening Milling

1. Introduction

Milling is a well-established manufacturing process for producing components with a defined geometry. In addition to the component geometry, milling of metallic materials produces a surface layer, which differs from the base materials in terms of hardness, grain morphology and microstructure as well as residual stresses [3–7]. A detailed examination of the material's property gradients after milling is of both academic and technical interest, since the material properties in the surface layer can be of decisive importance for component properties such as fatigue life and wear resistance [3–11]. In addition, the characterization of the hardness gradient in the near surface material volume enhances the comprehension of the machining process, facilitating optimization strategies for machining of difficult-to cut materials such as high manganese steels [12,13].

The increase in hardness of the near-surface material volume observed during milling compared to the initial state [3–5] is attributed to plastic deformation during machining. The thickness of the near-surface material volume influenced by milling is in the range of a few micrometres, making depth-resolved characterization of the local mechanical properties challenging, but possible with the aid of nanoindentation. In this context, high manganese TWinning Induced Plasticity (TWIP) steels are particularly suitable for characterising the hardness gradient in the material volume modified by milling, as a comparatively large increase in strength and hardness for metallic materials can be assumed in material areas that are plastically deformed during milling.

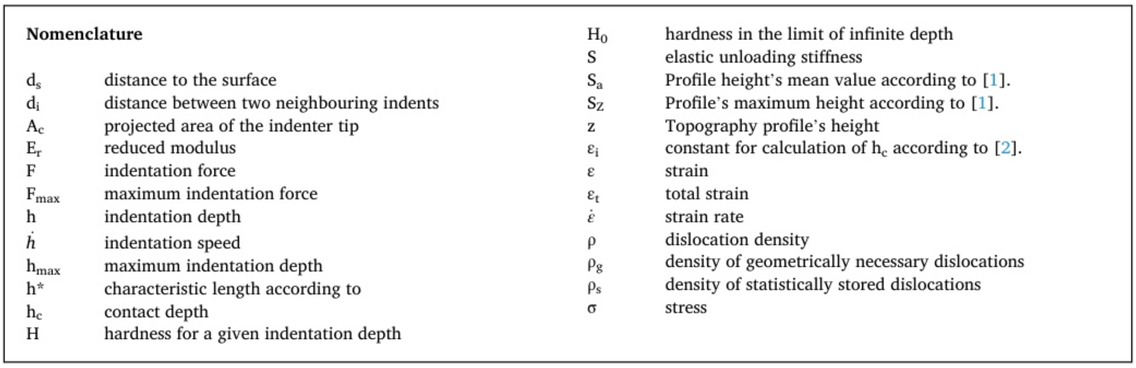

Nomenclature		H_0	hardness in the limit of infinite depth
		S	elastic unloading stiffness
d_s	distance to the surface	S_a	Profile height's mean value according to [1].
d_i	distance between two neighbouring indents	S_Z	Profile's maximum height according to [1].
A_c	projected area of the indenter tip	z	Topography profile's height
E_r	reduced modulus	ε_i	constant for calculation of h_c according to [2].
F	indentation force	ε	strain
F_{max}	maximum indentation force	ε_t	total strain
h	indentation depth	$\dot{\varepsilon}$	strain rate
$\dot{h}$	indentation speed	ρ	dislocation density
h_{max}	maximum indentation depth	ρ_g	density of geometrically necessary dislocations
h^*	characteristic length according to	ρ_s	density of statistically stored dislocations
h_c	contact depth	σ	stress
H	hardness for a given indentation depth		

The high, particularly quasi-static hardening potential of TWIP steels is largely due to the formation of twins during deformation, which reduces the dislocation mean free paths and is therefore named "dynamic Hall-Petch effect". A detailed overview of the TWIP effect and the properties of high manganese steels is provided by De Cooman et al. [14] and Bouaziz et al. [15]. The extent to which the TWIP effect occurs during milling has not yet been investigated in detail and elaboration of adequate hypotheses are challenging, since time-variant temperature, stress, strain and strain rate fields need to be considered [16].

For metallic materials in general and austenitic steels in particular, only limited work has been published on the depth-resolved characterization of the milling-induced hardness gradient in the near-surface material volume. Klein et al. [3] carried out instrumented cyclic indentation testing based on the work of Kramer et al. [17] on the high-manganese TWIP steel HSD®600 after up and down milling. Hereby, ten indentation cycles were performed on every measurement point with a maximum force was 1000 mN. The indentation tests were iteratively repeated after defined electrolytic polishing steps, so that after removing the near surface material volume established by up milling until to a depth of 54 μ m through 4 polishing steps, no difference to the base material was detected. The measured hardness decreases continuously from the surface to the base material. The increase in hardness due to up milling was approx. 10 % compared to the base material, whereas the increase in hardness in the case of down milling was approx. 5 %. It should be noted that the authors estimated the elastically-plastically deformed material depth to be up to 75 μ m based on Johnson's work [18], taking into account the indentation diagonal after ten cycles.

Further work on the characterization of the hardness gradient after up and down milling was carried out by Laamouri et al. [4] on the high-alloyed steel X160CrMoV12. In this work, instead of flat surfaces, V-shaped notches were milled. The authors characterised the depth-resolved hardness in the notch base through hardness measurements perpendicular to the surface with a load of 490.5 mN. It is neither detailed how the gradual material removal took place, nor how large the elastically-plastically deformed material volume was. For both up and down milling, a decreasing hardness curve from the surface to the base material was determined. While an increase in hardness of 75 % was induced on the surface compared to the base material during up milling, this increase was only 45 % after down milling. Furthermore, the transition from the hardened material volume to the base material was detected after up milling at a surface distance of 300 μ m, whereas in case of down milling a hardness increase was only detected until to a depth of 50 μm.

In addition to the work on high-manganese TWIP steel HSD®600 and on the high-alloy steel X160CrMoV12, the work of Yao et al. [4,5] on titanium alloy TB6 deals with the near surface hardness gradient after milling. However, the authors do not detail the sample preparation for this investigation, but an iterative material removal can be assumed, since the first measured value is given directly on the surface. Besides, it is not specified whether the measurement was carried out on the circumferentially milled or face-milled side, although a measurement on the face-milled side is likely due to the sample geometry. Using a load of 245.25 mN and a gradual increase of the surface distance by 10 μ m during their measurements, the authors determined a depth-resolved hardness curve after milling. Here, an increase in hardness of approx. 15 % compared to the base material up to a surface distance of 30–40 μm with a continuous decrease from the surface to the base material in agreement with the results of Laamouri et al. [4] and Klein et al. [3] was detected.

Besides the work by Klein et al. [3], studies on the hardness change due to machining of austenitic steel are only available for cryogenic turning of the corrosion-resistant steels AISI 347 [7,8,19] and AISI 904L [7] with external CO_2 cooling [7,8,19] or a metal working fluid based on monoethylene glycol [7]

In this context, Boemke [7], Skorupski et al. [8] and Mayer et al. [19] carried out microhardness measurements in cross sections with a maximum indentation force of 100 mN, whereby the minimum distance to the surface was at least 20 μ m. In accordance with the work of Klein et al. [3], a decreasing hardness with increasing surface distance was determined, whereby the properties of the base material were reached at a depth of between 150 μ m and 400 μ m. Consequently, the depth of the turning induced hardened material was greater than after milling of TWIP steel HSD®600 [3]. The maximum hardness measured at a surface distance of 20 μ m differed depending on the feed rate and was up to twice as high as that of the base material. In comparison to the work on austenitic steels, the hardness curve measured by Guo and Sahni [20] in the cross-section of AISI 52100 after hard turning with a load of 245,25 mN is of interest. Up to a surface distance of approx. 20 μ m, the authors identified a "white layer" that was 40 % harder than the base material, while a "dark layer" that was approx. 10 % softer was determined at a surface distance of approx. 20 μ m–40 μ m. Consequently, the turning induced hardness variations and the depth of the modified material volume was greater for the initially softer AISI 347 than for the initially harder AISI 52100. Thus, the material's mechanical properties influence the depth and hardness increase by machining. In contrast to all previously mentioned studies [3,4,8,19, 20], Javidi et al. [21] found no increase in hardness in the near-surface region after conventional turning of 34CrNiMo6, whereby the minimum distance to the surface was approx. 10 μ m. In this study, sections transverse to the cutting direction and along the feed direction were studied with a maximum indentation force of 100 mN.

Oevermann et al. [9] investigated the increase in hardness after deep rolling at room temperature and 550 ° C on the hardness HV0.2 of the high-manganese TWIP steel X40MnCrAl19-2. Although deep rolling differs fundamentally from milling, the observation of the increase in hardness and hardness gradient is of interest since the same material was investigated in the present study. At the smallest surface distance of 100 μm examined in this study, the increase in hardness compared to the base material was approx. 75 %. Furthermore, the hardness decreases continuously with increasing surface distance, which is analogous to the situation found after milling [3–5]. The thickness of the hardened zone was approx. 1000 μm. Considering the beforementioned studies on hardness in the surface layer after machining, it can be assumed that the thickness of the hardened zone after deep rolling is significantly greater than after up or down milling.

To increase the resolution of hardness gradient in depth direction, the smallest possible forces and penetration depths should be applied. During measurements with indentation depth h <1000 nm, indenter tip impressions become too small for precise area determination through light optical imaging. Thus, the hardness is determined based on the indentation force F- indentation depth h curves. The model proposed by Oliver and Pharr [2,22] has been widely used for this purpose. As this model was used in the present study, the basic principles are briefly summarised for the convenience of the reader. In this model, the contact depth hc is used for determination of the area used for hardness calculation. As schematically shown in Fig. 1a), it represents the length along which the indenter and the material to be tested are in contact projected in loading direction. It is derived from the force-displacement curve through equation (1)which is represented geometrically in Fig. 1a). Hereby, the stiffness S represents the slope of the F-h-curve during unloading near F_{max}. εi is a constant depending on the indenter tip geometry and, in the present work, εi =0,75 as a Berkovich indenter was used.

The area of the indenter tip in contact with the tested material pro

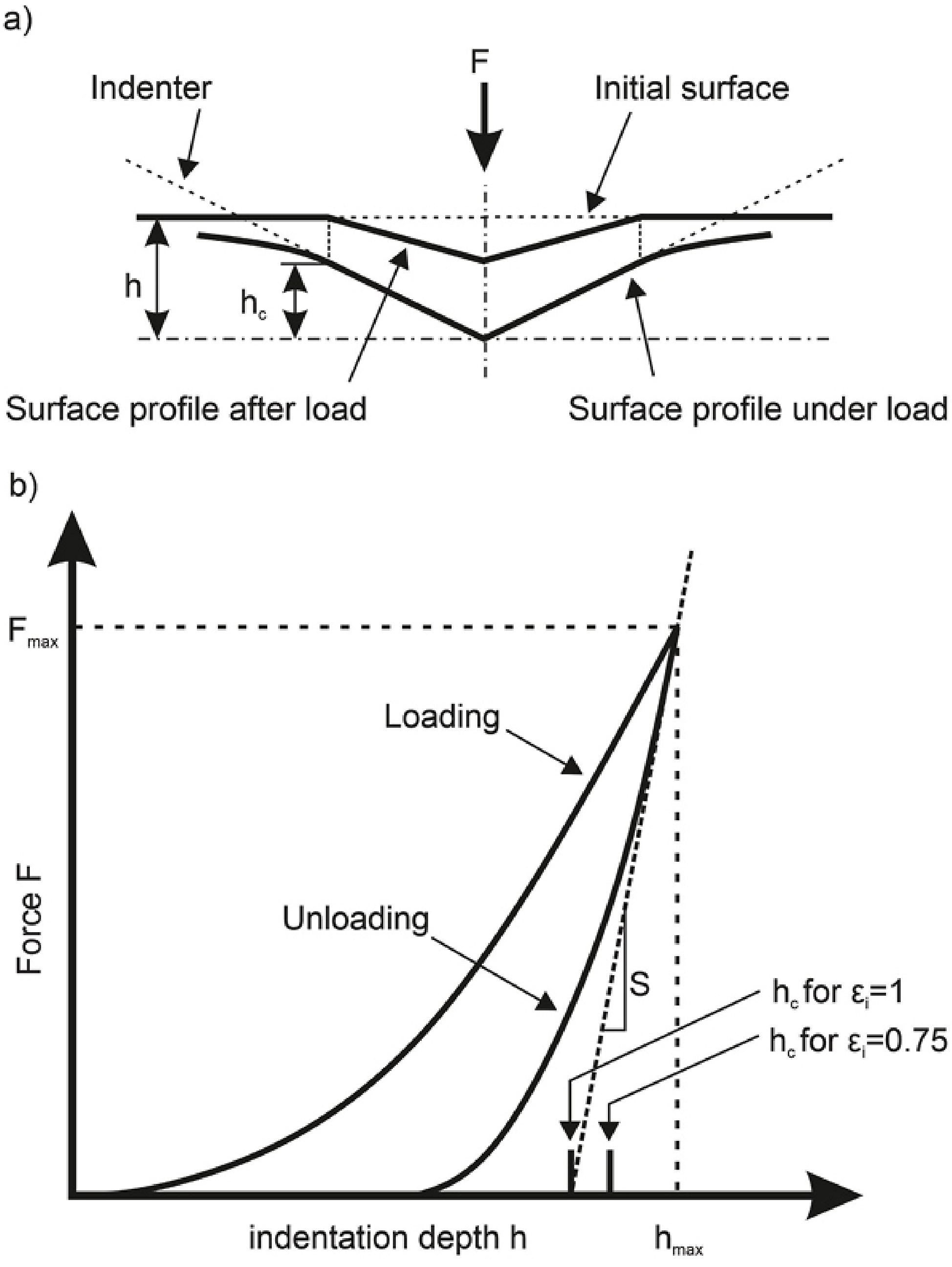

Fig. 1. a) Schematic representation of indentation depth h and contact depth hc during indentation and b) determination of hc based on the Force F – indentation depth h curve adapted from Ref. [2].

jected into a plane perpendicular to the load direction Ac is as a function of the contact depth hc which is determined through a calibration procedure. During subsequent indentations in various materials, Ac can be calculated based on hc, so that hardness H is determined through equation (2).

$$h_c = h_{max} - \varepsilon_i (F_{max} / S) \qquad \text{(Eq. 1)}$$

$$H = F_{max} / A_c \qquad \text{(Eq. 2)}$$

Thus, hardness is calculated based on the projected contact area at maximum indentation force instead of the conventional determination based on the projected area of the indent after unloading. Nevertheless, Oliver and Pharr [2] showed that their approach leads to results which are in excellent agreement to those determined via conventional area determination.

Besides challenges regarding area determination, indentation depths h <approx. 1000 nm [22] with self-similar bodies such as Berkovic tips result in an increase in hardness with decreasing indentation depth, which is described as the indentation size effect. Pharr et al. [22] and Voyiadjis and Yaghoobi [23], for example, provide an overview of the large number of studies investigating this phenomenon. Among other aspects, the authors discuss the highly regarded model by Nix and Gao [24], which explains the indentation size effect for a conical tip on the basis of geometrically necessary dislocations. For this purpose, Nix and Gao [24] calculate the length of the geometrically necessary dislocation rings as a function of the indentation depth based on the geometry of the indenter tip. It is assumed that the geometrically necessary dislocations are located below the tip within a hemisphere with the radius of the indent at the surface [24]. In addition, a relationship is established between the shear yield stress and the dislocation density according to Taylor’s relation, the shear stress is converted into a normal stress using the von Mises flow rule and the normal stress is converted into a hardness using Tabor’s factor [21]. This results in Eq. (3), delineating the ratio of hardness H and the theoretical hardness H0, resulting exclusively from the statistically distributed dislocations without geometrically necessary dislocations, as a function of the ratio of the scaling variable h* and the indentation depth h [24]. Note that h* is constant during indentation but a function of the indenter geometry and the density of the statistically distributed dislocations in the tested material.

$$\mathrm{H} \Big/ H_0 = \sqrt{1 + (h^* / h)} \qquad \text{(Eq. 3)}$$

In the context of the indentation size effect, the technique of continuous stiffness measurement (CSM) is particularly useful as it allows continuous, contact depth-resolved measurement of the reduced modulus and hardness. Hereby, the indentation depth or indentation force is superimposed with an oscillating movement of a small amplitude compared to the total indentation force or indentation depth, respectively. A sufficiently large amplitude of the oscillating force enables a determination of the stiffness during loading and consequently a contact depth- resolved determination of reduced modulus and hardness. A detailed overview of CSM and the various fields of application can be found in Ref. [25].

2. Materials and methods

In the present study, the high-manganese TWIP steel 1.7401 from thyssenkrupp Hohenlimburg GmbH was analysed. The sheet material with a thickness of 6.0 mm was hot rolled, pickled, oiled and skimmed into sheets with a width of 645 mm and a length of 1200 mm. Its chemical composition given in Table 1was measured by optical spectral analysis. A stacking fault energy of 26 mJ/m2 at room temperature was calculated based on the chemical composition using the model of Curtze et al. [26].

The TWIP steel exhibits a fully austenitic microstructure with a homogeneous distribution of the equivalent grain diameters as shown in

Table 1

Chemical composition of the investigated TWIP steel 1.7401 measured by optical spectral analysis.

Alloying element	C	Mn	Cr	Al	Si	Ti	P	S	Ni	Mo	Cu	Fe
Content in wt.-%	0.36	19,64	1,63	1,16	0,31	0,03	0,02	0,01	0,06	0,25	0,04	rest

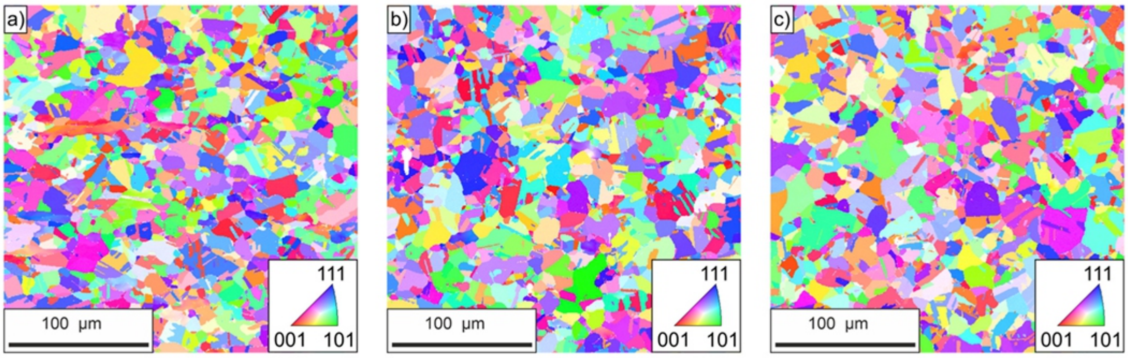

Fig. 2. Inverse Pole Figure maps of high manganese TWIP steel 1.7401 in the initial state investigating a) a cross section along the rolling direction b) a cross section transverse to the rolling direction and c) a section parallel to the rolling skin.

Fig. 2. The material's biggest equivalent grain diameter is about 30 µm and the average equivalent grain diameter is approximately 11 µm.

To investigate the uniaxial quasi-static behaviour of the test material, four specimens designed in accordance to DIN EN ISO 6892-1 [27] were water jet cut from the sheet material. The quasi-static behaviour of the test material was characterised on a Zwick/Roell Z250 tensile testing machine from Zwick Roell (Ulm, Germany) with a strain rate of ˙ ε=0, 25*10 3 1 s in accordance to DIN EN ISO 6892-1 [27]. The specimen temperature was measured during the tensile tests in the centre of the gauge section using a type K thermocouple. In addition, tensile tests were carried out up to a defined total elongation of εt =15 %, 30 %, 45 %, 60 % and until fracture to determine the increase in hardness as a function of the uniaxial quasistatic deformation. Samples were then taken from the gauge length section and specimens for nanoindentation were produced by grinding and mechanical polishing, whereby a suspension with a grain size <40 nm was finally used. Hereby, the specimens were prepared longitudinally (LS) and transversely (CS) to the loading direction during prior monotonic deformation.

For production of specimens with milled surfaces, waterjet cut sample blanks with an overmeasure of 1 mm in the gauge length were firstly made. From these blanks, fatigue specimens were produced by up and down milling on all four sides of the gauge length until the geometry given in Fig. 3was achieved. Note that the results of fatigue testing will be published elsewhere. Since the machining of high manganese steel has hardly been researched, the milling parameters successfully used by Klein et al. [3] to machine the high manganese steel HSD®600, given in Table 2, were applied. In addition to the specimens with milled surface, an up milled sample was electrolytically polished using a Polectrol

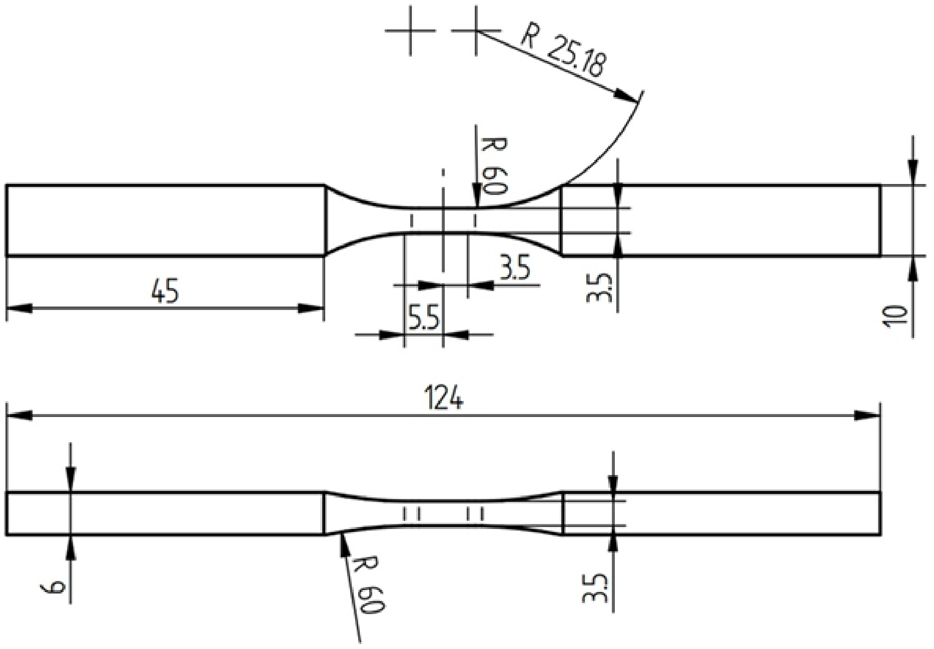

Fig. 3. Geometry of the milled fatigue specimens before sample preparation for nanoindentation.

device and electrolyte A3, both by Struers GmbH (Willich, Germany). To polish only the gauge length and the transition radius, the sample shafts were masked with adhesive tape. The polishing process was then carried out for 15 s with an electrical voltage of 30 V. Note that the samples with rolling skin were only milled on the waterjet cut sides, but only the side with rolling skin is of importance for the present work.

Topography measurements were conducted using a confocal microscope “µsurf explorer” from NanoFocus AG (Oberhausen, Germany). Focused Ion Beam cuts were established and documented with a “GAIA3” FIB-SEM system produced by Tescan s.r.o. (Brno, Czech Republic), which was also used for scanning electron microscopy and Electron Backscatter Diffraction (EBSD) measurements using an EBSD camera “Hikari-Plus” from Ametec Inc. (Berwyn, USA). The indentation tests were performed using a nanoindenter type "FT-I04" from FemtoTools AG (Buchs, Switzerland), equipped with a FT-S20.000 sensor capable of measuring forces up to 20 mN and featuring a Berkovic tip made of diamond.

The data analysis for hardness calculation according to the model of Oliver and Pharr [2,22] was automated in the operating software for conventional single indentation as well as for CSM. The indentation was carried out with controlled penetration depth h and an indentation speed of $\dot{h}$=100nm/s for both conventional single indentation and CSM. In case of conventional single indentation, various series of measurements were carried out with maximum indentation depths h_{max} = 50 nm, 100 nm and 200 nm. The dwell time was 0.1 s and the unloading speed was 50 nm/s. In case of CSM, the maximum penetration depth was always h_{max} =200 nm and the superimposed oscillation of the tip for continuous stiffness measurement was performed with an amplitude of 2 nm and a frequency of 150 Hz. Furthermore, no hold time was performed, and the unloading speed of 10 µm/s was significantly faster than for single indentations, as the unloading after reaching hmax is not relevant for determining the stiffness during CSM.

Table 2

Milling parameters used during up and down milling.

Revolutions per minute	Feed per tooth in mm	Cutting width in mm	teeth	Tool coating
5091	0.025	0.1	4	AlTiN

The area function of the tip A =f(hc) according to Ref. [2] was verified using CSM on a fused silica sample, which was supplied with the nanoindenter. The sample exhibits a hardness of 9.434 GPa and the combination of sample and diamond tip results in a reduced modulus Er =70.25 GPa. In this sample, 20 indentation depth controlled CSM were carried out with an indentation speed of $\dot{h}$ =0.012 µm/s. The superimposed oscillation movement of the indenter was performed with an amplitude of 2 nm and a frequency of 150 Hz. The measurement was ended at the maximum indentation force of the measuring head of 20 mN. This results in the H-hc- and reduced modulus Er-hc curves shown in Fig. 4.

For hc ≥40 nm, the variation of the Er-hc and H-hc curves is significantly smaller than the standard deviation, so that a reliable measurement is guaranteed. Between hc =40 nm and hc =15 nm, the standard deviation increases by less than a factor of two and the arithmetic average at a given hc deviates stronger from the expected value than for larger hc, but only by a maximum of 1 % which is tolerable. Thus, this range can be used reasonably but it is slightly less reliable than in case of hc ≥40 nm. For hc <15 nm, the deviation from Er and hc from the known fused silica's properties is such pronounced that measurements in this range were not considered in this study. These deviations can be attributed to tip rounding.

Sample preparation aiming the characterization of the milling- induced hardness gradient by nanoindentation was realised through cutting out the fatigue samples' gauge lengths in a first step. Then, an approx. 60 µm thick nickel layer was applied to the milled surface by electrolytic plating. Metallographic sections were then produced by grinding and mechanical polishing. The smallest grain size of the polishing paste was 1 µm, because polishing with a smaller grain size resulted in a gap between the nickel layer and the TWIP steel. However, this preparation method resulted in a sufficiently smooth topography with Sa <10 nm. For milled samples, sections perpendicular to the feed direction are termed cross sections, while the longitudinal section is orientated along the feed direction as schematically represented in Fig. 5 a). Note, that the feed direction was perpendicular to the rolling direction. The polished sample was only investigated in a section transverse to the feed direction of previous up milling and the rolling skin was investigated in a section longitudinal to the rolling direction.

Conventional single indentation as well as Continuous Stiffness Measurements (CSM) were performed 40 times for each material state to determine the arithmetic mean as well as the empirical standard deviation of the hardness. Hence, 40 measurements were performed for one data point indicating the hardness of the initial state or themonotonically deformed material volume. For hardness gradient determination in the near surface material volume, 40 measurement points were investigated for each distance to the surface ds indicated, so that 40 indent lines from the nickel layer to the bulk material schematically represented in Fig. 5b) were recorded for each combination of h_{max} and di. The indentation positions were defined using an integrated optical microscope. Due to small position shifts of <3 µm between the defined spot and the actual indentation spot due to imperfections during position calibration, the position of the indentations was checked after each measurement using the integrated optical microscope for hmax ≥ 50 nm. The positions of indents for hmax =25 nm were verified using the beforementioned “GAIA3” FIB-SEM system. Furthermore, nickel coating and the TWIP steel cannot be distinguished through examination of Er as they do not differ significantly resulting in a necessity of indent position verification through light optical microscopy. Therefore, the beforementioned procedure using the light optical microscope was used. Note that no relevant deviation from the distance di between to neighbouring indents occurred. In case of distances between the nickel layer and the middle of an indent <0.5 di, the respective measurement was not considered valid due to the possible influence of the nickel layer on the measured hardness. In that case, the subsequent indent was the first to be considered for hardness gradient determination. Hence, the indicated surface distance accuracy is Δds = ±0,5 di.

3. Results

3.1. Hardness after uniaxial quasi-static deformation

The monotonic stress-strain curve of the investigated high- manganese TWIP steel is shown in Fig. 6for one representative specimen. The TWIP steel exhibits a tensile strength of 875 ±6 MPa, a yield strength Rp0.2 of 353.6 ±6.5 MPa and an elongation at fracture of 69 % ±1 %.

Fig. 7shows the hardness of the material as a function of the uniaxial deformation. As mentioned before, the material was deformed up to the indicated total elongations εt. Note that the plastic deformation after unloading is smaller due to reversible elastic deformation. Nevertheless, the respective material states are differentiated according to the applied total elongation εt. For εt ≤60 %, higher strains result in higher hardness. At εt =15 %, the gradient of the H-εt curve exhibits an increase, reaching a relatively stable plateau between εt =15 % and εt =45 %. Subsequently, a slight decrease in slope is observed, with hardness approximately maintaining a constant level for εt ≥60 %, considering the inherent scatter in the data. Furthermore, the hardness differences between the longitudinal and cross sections for a given εt are significantly smaller than the scatter.

In addition to the conventional indentation, H-hc curves of the

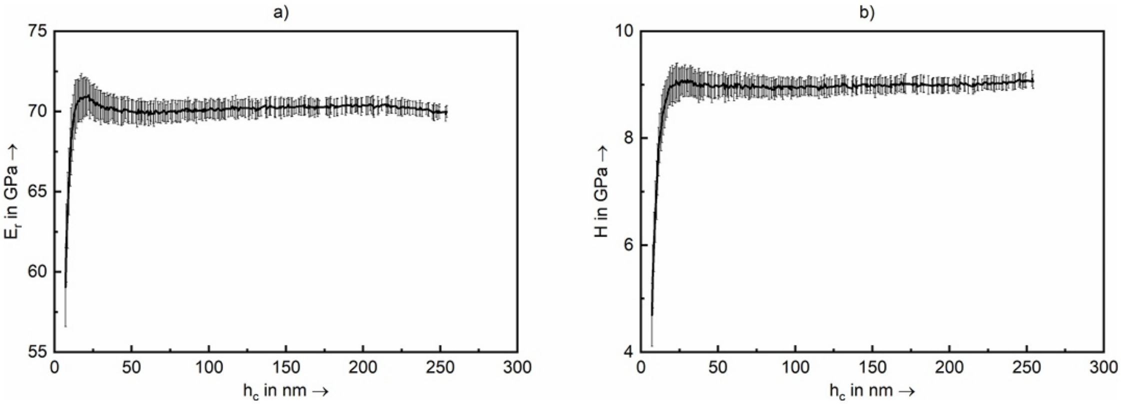

Fig. 4. a) Reduced Modulus and b) Hardness as a function of contact depth for the Calibration sample made of fused silica.

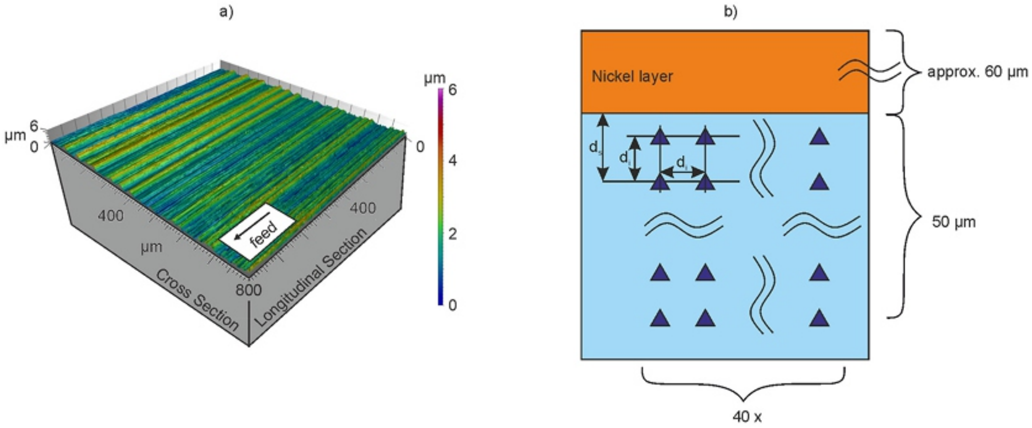

Fig. 5. a) Illustration of the orientation of cross and longitudinal section with respect to the feed direction and b) schematic representation of the indent positioning and related parameters ds and di.

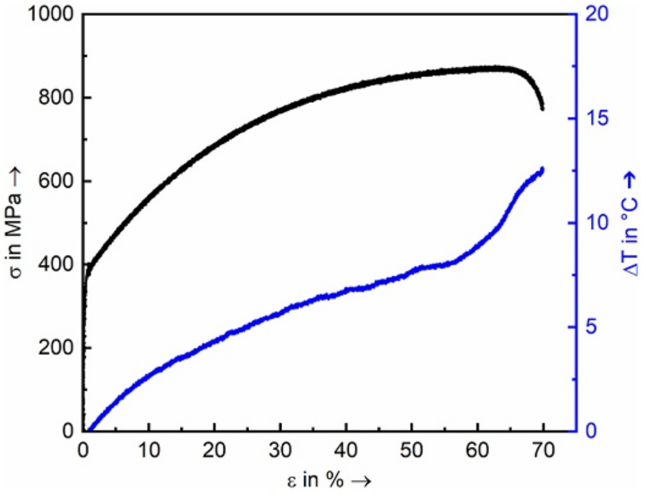

Fig. 6. Monotonic stress-strain curve of the investigated 1.7401 as well as corresponding change in specimens' temperature in the middle of the gage length ΔT.

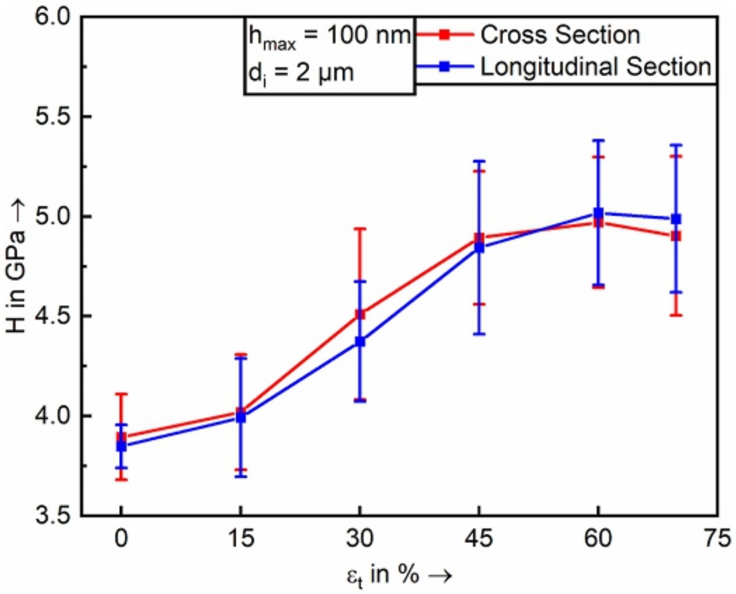

Fig. 7. Hardness of 1.7401 as a function of uniaxial straining through quasi static tension loading.

investigated material in the initial state as well as after monotonic deformation shown in Fig. 8 were determined using CSM in order to measure the influence of the contact depth on the hardness continuously. In the initial state, H declines with increasing hc from approx. 4 GPa to approx. 3 GPa in a degressive way. A larger deformation before indentation always results not only in higher hardness, but also in a

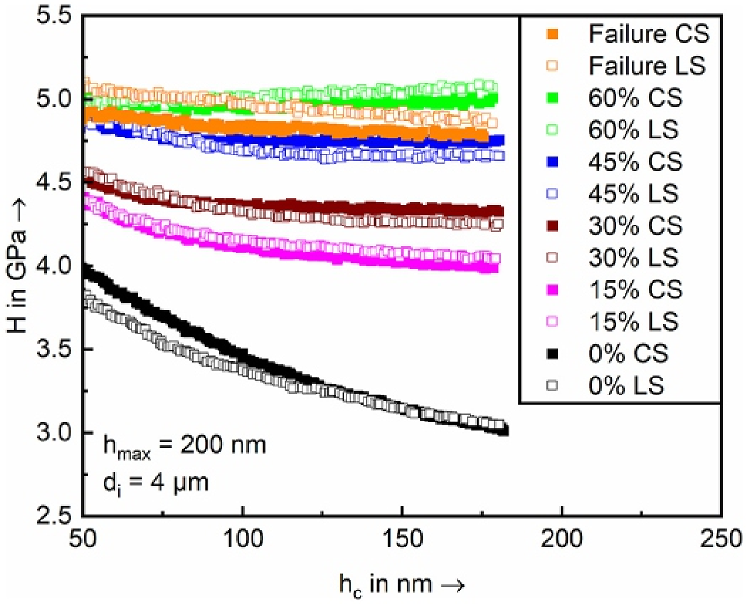

Fig. 8. Hardness as a function of contact depth of 1.7401 in the longitudinal and cross section after tensile deformation to different total strains.

smaller decrease in hardness with increasing hc, resulting in approximately linear curves with -if any- small slope for ε t ≥ 60 %. Consequently, bigger differences in hardness are measured between the various deformation states at larger hc .

For clarity, the curves including the scatter of H for the initial state and εt =30 and 60 % are shown in Fig. 9 for the cross and longitudinal sections. The difference between the H-hc curves of the cross and longitudinal section is always significantly smaller than the scatter of H. For εt =60 %, the scatter of H is bigger than the difference to the mean value curves for εt =45 %, and the material condition after specimen failure, besides clear differences between εt = 45 % and εt = 60 % regarding mean values, revealing that at least 40 measurement points are necessary for determination of meaningful differences. Furthermore, the H mean values and empirical standard deviation determined via CSM coincides with the values determined using conventional single indentation for all deformation states in case of comparable hc , making CSM with the used parameters a reliable procedure.

In analogy to the H-hc curves, the E r-hc curves given in Fig. 10 were determined for the initial state as well as after monotonic deformation. The material in the initial state, as well as after monotonic deformation, shows similar curves. Moreover, the curves of the cross and longitudinal section are similar, too. The reduced modulus varies between 160 Gpa and 170 MPa with a tendency to higher values in case of larger hc. However, the change in Er as a function of hc is s lower than the scatter inEr given in Fig. 11 for the cross and longitudinal section of the initialstate as well as t =30 % and εt =60 %.

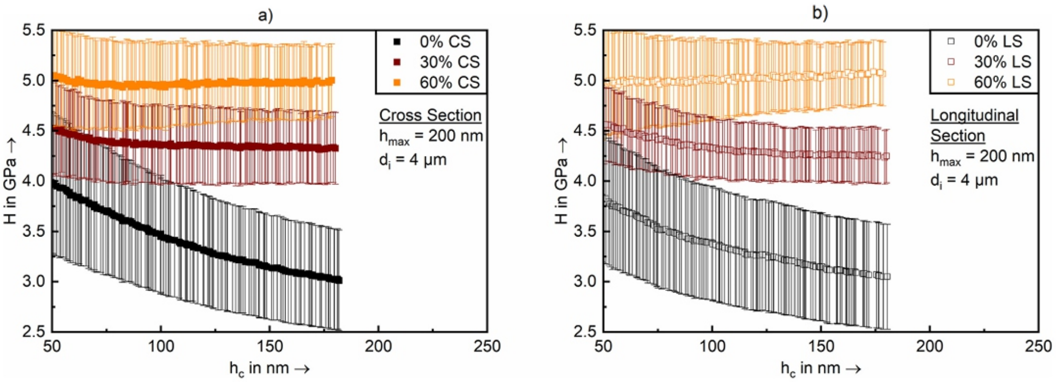

Fig. 9. Hardness as a function of contact depth including scatter for in the initial state and after tensile deformation until 30 % and 60 % for a) the longitudinal section and b) the cross section.

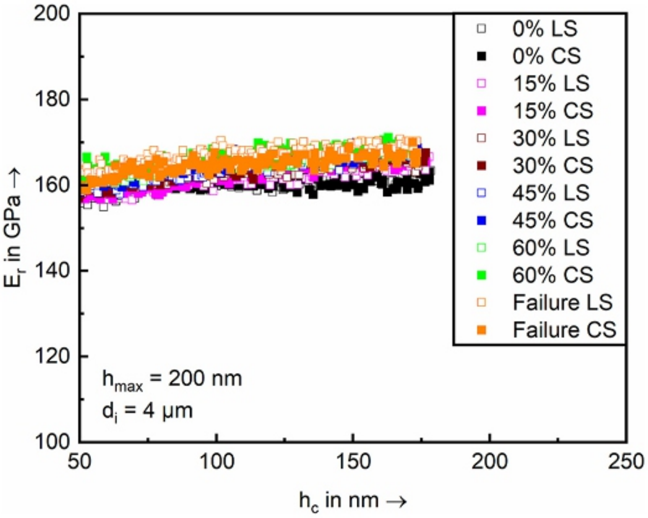

Fig. 10. Reduced modulus as a function of contact depth of 1.7401 in the longitudinal and cross section after tensile deformation to different total strains.

3.2. Surface topography and near surface grain structure of surface morphologies

The topographies of the analysed sample surfaces are shown in Fig. 12 and the resulting roughness parameter SZ representing the profile's maximum height [1] as well as the profile height's arithmetic mean value S_a determined according to Eq. (4) [1] are given in Table 3 [1].

$$S_a = \frac{1}{A}\int\int_A \left| z(x_1y) \right| dxdy \qquad \text{(Eq. 4)}$$

The rolling skin exhibits the roughest surface, while the milled samples show comparable topographies and thus roughness parameters. In case of the surface produced by up milling, a stronger ripple due to movement of the milling tool in feed direction occurs compared to the surface produced by up milling. Transverse to the feed-related ripple, a surface structure composed of alternating peaks and valleys extends uniformly along the feed direction across the entire measured length. However, the distance between peaks and valleys is approximately three times smaller compared to the feed-related ripple. The formation of this surface structure can be explained by the milling tool's cutting edge topography. In the case of the sample which was electrolytically polished subsequent to up milling, the feed-induced ripple was removed and the surface structure transverse to the feed direction is characterised by a greater peak-to-peak distance than that of the milled samples. Furthermore, pits with a diameter < 200 μm can be recognised, revealing locally higher material removal.

Focused Ion Beam (FIB) sections were made after specimen manufacturing orthogonal to the surface to characterize the near surface grain structure. Note that the cut surface was for all specimens along the loading axis of the fatigue specimens and thus along the feed direction for the milled surfaces as well as the polished specimen and transverse to the rolling skin. Furthermore, a platinum-layer was applied before cutting to improve the FIB cut's quality in terms of topography. A

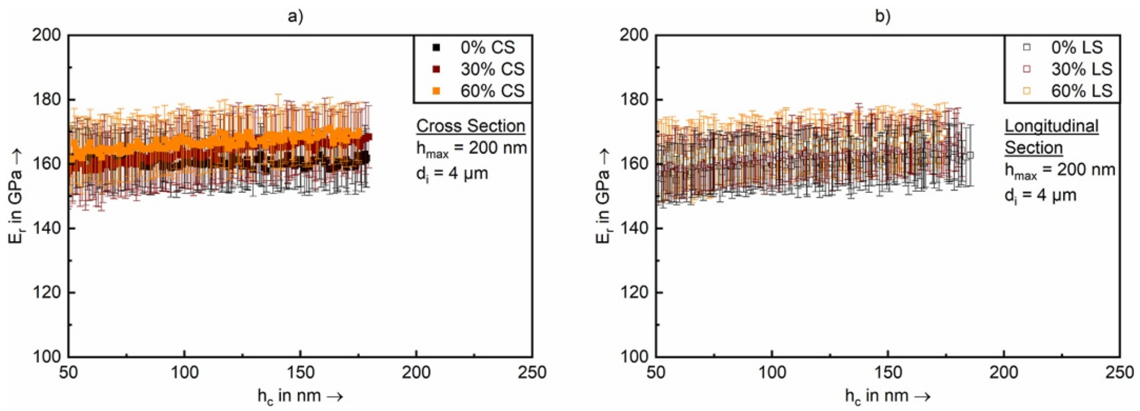

Fig. 11. Reduced modulus as a function of contact depth including scatter for in the initial state and after tensile deformation until 30 % and 60 % for a) the longitudinal section and b) the cross section.

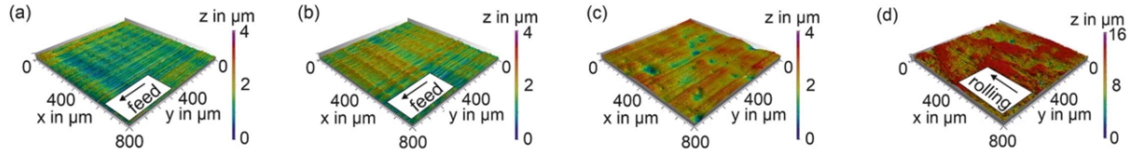

Fig. 12. Topography of the surface morphology after a) up milling b) down milling c) up milling and subsequent electrolytical polishing as well as d) rolling.

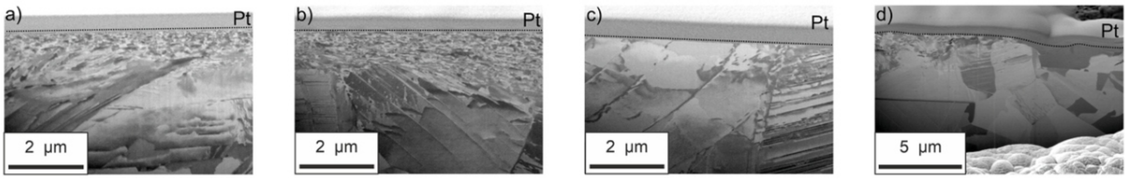

Fig. 13. Cross sections obtained by FIB techniques showing the grain structure within the near surface material after a) up milling b) down milling c) up milling and subsequently electrolytical polishing and d) rolling.

Table 3

Roughness parameters of the investigated surfaces.

Surface morphology	S_Z	S_a
Up milled	3.86	0.49
Down milled	4.18	0.54
Polished	4.79	0.80
Rolling skin	19.00	2.55

nanocrystalline layer with a thickness of 1–2 µm below the surface was detected in the milled specimens. Beneath the fine crystalline surface layer, material contrast variations reveal elongated, line-like regions with widths in the nanometre range. These regions, coarser than the fine-grained surface layer, indicate plastic deformation beneath the nanocrystalline structures. Accordingly, these structures could represent deformation twins or dislocation structures, which could only be clearly analysed with further investigations that go beyond the scope of the present work, such as a determination of the local grain orientation by means of transmission electron microscopy. The polished specimen is devoid of a nanocrystalline surface layer, but the line-like regions remain intact. The rolling skin shows only locally finer-grained areas near the surface compared to the base material, but these are more inhomogeneous regarding their thickness and grain size than the nanocrystalline layers of the milled surfaces. Furthermore, the maximum depth of the finer-grained areas is approx. 5 µm.

3.3. Determination of parameters for the characterization of the near surface hardness gradient

The indentation size effect shown in section 4.1 leads to a conflict of interest when choosing the indentation depth: Smaller h_{max} enable closer spacing between successive indentations and a closer positioning of the indents to the surface, thus providing a finer resolution of hardness gradients within the zone of interest. However, smaller h_{max} lead to smaller hardness differences between differently deformed material due to the indentation size effect according to section 4.1, which is undesirable when characterising hardness gradients. To determine the impact of the indentation size effect on the measured milling-induced hardness gradient, the near-surface material volume after up milling was examined perpendicular to the feed direction. This approach, as opposed to cutting along the feed direction, minimizes the likelihood of hardness gradients within a cut, attributed to the intermittent cutting action during circumferential milling. The characterization of a section longitudinal to the feed direction is given in chapter 4.4.

In analogy to the investigations on the uniaxially deformed TWIP steel, CSM was used to investigate the indentation size effect through determination of H-hc curves for different distances to the surface ds. Fig. 14a) shows H-ds curves for hmax =200 nm, 100 nm and 50 nm, revealing a hardness gradient for all hmax such that the hardness degressively decreases with increasing ds and asymptotically transitions to the H of the base material. Fig. 14b) details the influence of hc on H through continuous H-hc curves for different ds. H exhibits minimal decreases with increasing hc for ds =4 µm, indicating a negligible influence of hc on the measured H. For ds ≥8 µm, H decreases as a function of hc and the decrease in hardness is bigger for larger ds. The closer the curves were determined to the surfaces, the greater the of increasing ds on the H-hc curves. Thus, differences between softer and harder material volume become smaller with decreasing hc. Moreover, the detection of the transition area from the hardened zone to the base material is less precise for smaller h_{max}: In case of h_{max} =50 nm, H is comparable between ds =16 µm and ds =24 µm, while a decrease of H is detected between ds =16 µm and ds =20 µm for h_{max} =100 nm as well as h_{max} =200 nm. Therefore, h_{max} =100 nm was chosen as a suitable compromise between resolution in H and ds.

For clarity, the H-hc curves including standard deviation are shown in Fig. 15for four surface distances within the zone of milling-induced hardness increase. The scatter of the measurements for ds =4 µm and 8 µm is about twice as large as for the base material at ds =28 µm. Furthermore, the scatter for ds =4 µm and 8 µm is approx. 1/3 of the difference in hardness between ds =4 µm and ds =28 µm.

To increase the resolution of the hardness gradient within the hardened zone, the possibility of reducing the di/h_{max} ratio for single indentation and h_{max} =100 nm was investigated. For this purpose, the H-ds curves in the near-surface material volume produced by up milling was determined in a section transverse to the feed direction. Considering the work of Phani et al. [28], di/h_{max} ratios of 20, 15 and 10 were selected. The H-ds curves for the different di/hmax ratios are shown in Fig. 16. For all curves, the trend is identical and the differences between the curves do not exceed the scatter at any ds. While the curve for di/h_{max} =15 is shifted by approx. 100 MPa respectively 3 % towards smaller values compared to that of di/h_{max} =20, the curve for di/h_{max} = 10 is shifted by approx. 200 MPa or approx. 6 % to larger values for ds > 45 µm.

3.4. Influence of the cutting process on the hardness gradient in feed direction

During circumferential milling, the tool cuts the material

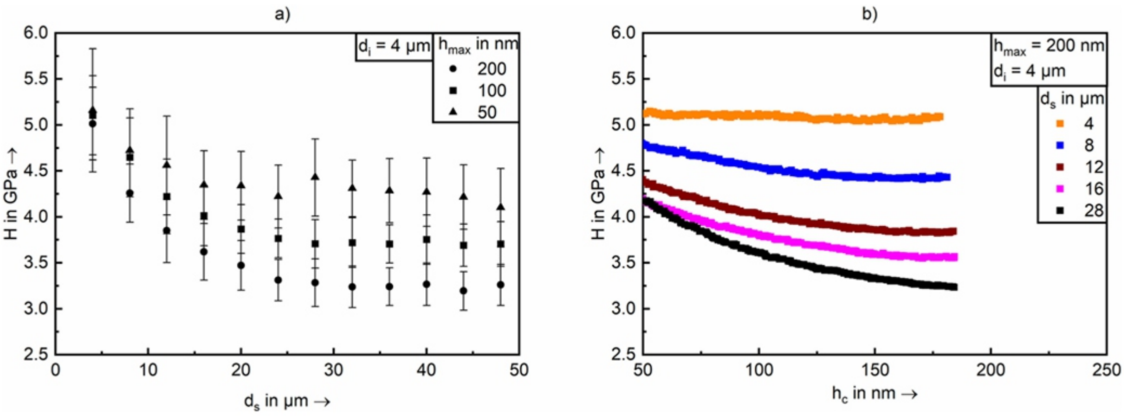

Fig. 14. a) Hardness H as a function of distance to the surface ds after up milling for three different

indentation depth and b) Hardness H as a function of contact depth hc for five different distances to the surface.

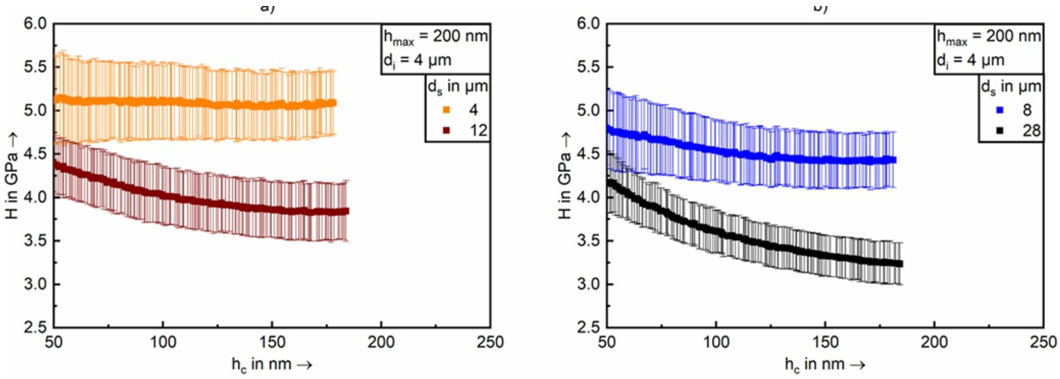

Fig. 15. Hardness as a function of indentation depth including scatter for four different distances to the up milled surface.

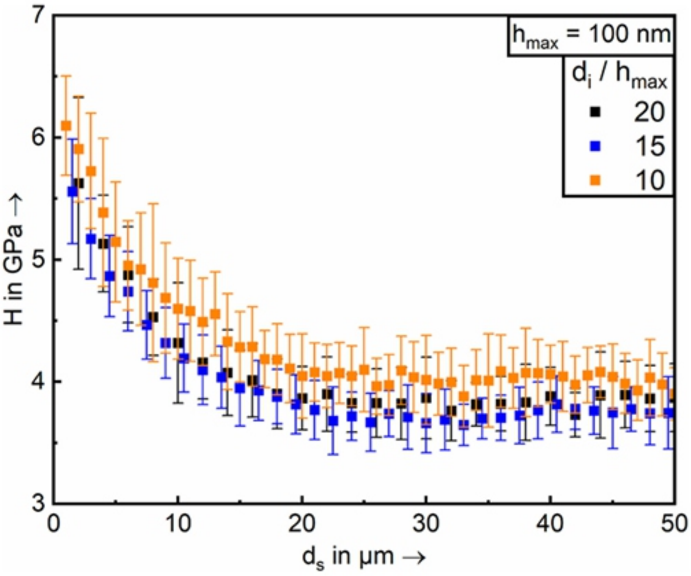

Fig. 16. Hardness as a function of the distance to the surface for a maximum indentation depth of 100 nm and three different step size to indentation depth ratios.

intermittently, so that the chip formation takes place discontinuously. In this respect, a hardness gradient in feed direction is possible. For this reason, the hardness gradient of the near-surface material volume produced by up milling was investigated not only transverse, but also along the feed direction. The H-ds curves in a section longitudinal to the feed direction are compared to the respective cross-sections' H-ds curves in Fig. 17. The curve for the longitudinal section tends to exhibit larger values than that for the cross section, particularly in the base material, whereby the differences are in the range of the standard deviation of the individual measuring points or even smaller.

In addition to the curves shown in Fig. 17, ten indent lines transverse

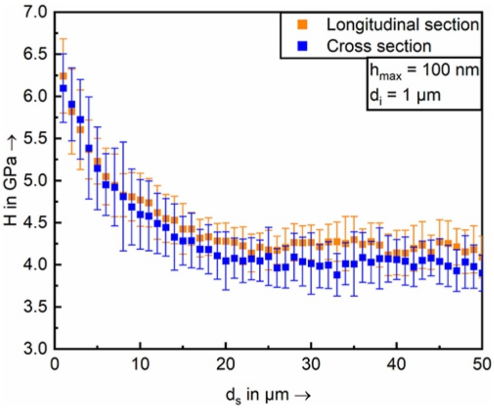

Fig. 17. Up milling induced hardness gradient measured in a section perpendicular to the feed direction (cross section) and in a section in feed direction (longitudinal section).

to the feed direction were made within the feed length, which was 100 µm, so that the indent lines exhibited a distance of 10 µm to the neighbouring indent line. The resulting H values along the feed direction are represented in in Fig. 18for five different distances to the surface (ds =1 µm, 2 µm, 3 µm, 9 µm and 40 µm). In accordance with the mean values shown in Fig. 17, no trend such as an increase or decrease in hardness as a function the position within the cut occurs. Hence, the milling tool's movement does not result in a significant hardness gradient in feed direction.

3.5. Characterization of the hardness of the nanocrystalline surface layer

According to the FIB cuts shown in Fig. 13, the milled sample exhibits a fine crystalline layer directly below the surface, which changes discontinuously into a coarser-grained structure. Considering the Hall- Petch relationship, a discontinuous change in hardness is possible where the grain size increases discontinuously. As the fine crystalline layer exhibits a thickness of approx. 1–2 µm, characterising the hardness gradient in this layer is challenging and not possible with the test parameters used in the previous series of measurements. Thus, additional measurements were carried out with hmax =25 nm, di/hmax =10 and consequently di =250 nm in the cross-section of an up milled sample. The indents were assigned to the nickel layer or the TWIP steel respectively using SEM images so that the ds were determined reliably. The H- ds curve resulting from this measurement procedure is shown in Fig. 19. No change in hardness can be determined up to a surface distance of approx. 1.25 µm. Subsequently, the hardness decreases with increasing ds continuously, but no sharp hardness drops at the transition from the fine crystalline layer to the coarser-grained structure are found.

4. Discussion

The extent to which uniaxial quasi-static deformation influences H was investigated. Considering the monotonic stress-strain curves in Fig. 6, the hardness increases substantially for εt ≤45 % with increasing deformation, so that that the quasi-static hardening affects the H determined by means of nanoindentation. Hereby, the differences between the longitudinal and cross sections are smaller than the standard deviation, so that no significant difference was detected. However, the difference in H between εt =0 % and εt =15 % is small compared to the monotonic hardening according to the stress-strain curve shown in Fig. 6. Therefore, an influence of indentation induced strain [29] and associated dislocation density [24,29,30] is likely. Hence, the comparatively small H differences with increasing monotonic deformation are likely to be affected by a maximum dislocation density. This is reached

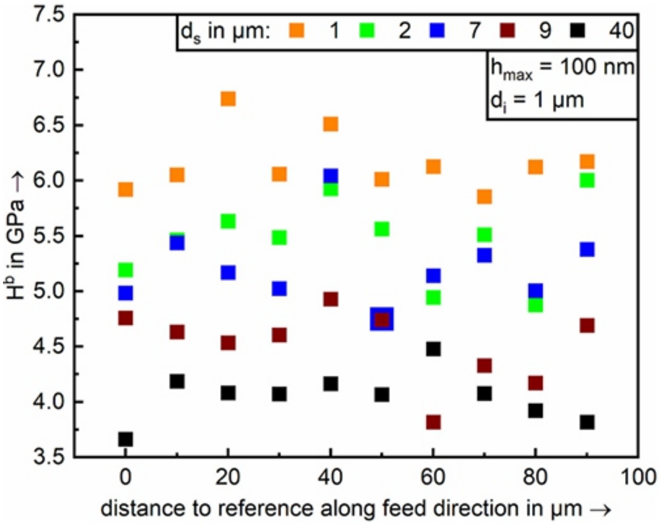

Fig. 18. Hardness distribution along the feed direction with a step size of 1/10 feed for four different distances to the surface.

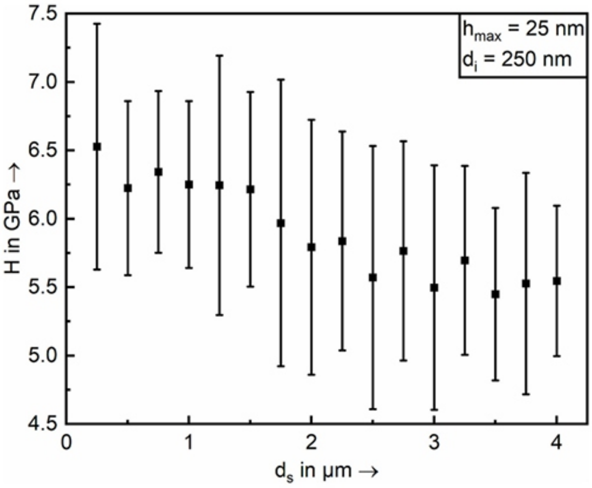

Fig. 19. Hardness evolution in a distance up to 4 µm for detailed characterization of the hardness within and close to the nanocrystalline surface layer established by up milling.

before specimen failure in the tensile test, due to the superposition of the indentation-induced deformation and the preliminary monotonic deformation. In this context, the H-hc-curves based on CSM measurements provide additional information to support the theory of geometrically necessary dislocations affecting H. To avoid redundancy, the influence of the monotonic deformation on the hardness is discussed using the continuous H-hc curves.

It is well known [23,24] that the indentation size effect occurs for hmax ≤1000 nm and is hence of importance in the present study considering h_{max} ≤200 nm. In this context, a detailed discussion of the H-hc curves based on CSM measurements is helpful. According to Figs. 8 and 9, H decreases from approximately 4 GPa–3 GPa between hc =50 nm and 200 nm, revealing a significant influence of hc on H. On top of that, a smaller decrease in H as a function of hc occurs in case of a larger uniaxial deformation before indentation. Thus, uniaxial deformation before indentation affects not only H, but also the slope of H-hc curves. Consequently, hc affects the relative differences in H between differently deformed parts of the material volume. Note that scatter of H is in the order of magnitude of the differences between the curves of e.g., εt =30 % and εt =45 %. Therefore, it is necessary to determine an average curve from 40 indents, as in the present study, or even more. The considerable scatter may be attributed to the comparatively small, superimposed oscillation amplitude of 2 nm, which has the potential to increase the influence of surface roughness on measured H. Further potential reasons include hardness differences due to the grain orientation distribution and potential orientation-dependent twining [31], as well as grain boundary effects.

In all deformation states, the H-hc curve’s trend is asymptotic, and it is appropriate to assume that H determined at h_{max} =200 nm in the present study differs by less than 10 % to the asymptotic limit.

The determination of H based on the model proposed by Oliver and Pharr does not consider pile-up or sink-in of material during indentation. However, the reduced modulus Er provides additional information about errors in determination of the contact are due to potential pile-up or sink-in effects. The average value of Er of approximately 165 GPa is coherent considering Eq. (5) and the diamond tip with Ei =1140 Mpa and νi =0,07 as well as the TWIP steel’s young’s modulus E =182 MPa determined via tensile testing and ν =0,24 [32–34]. According to Figs. 10 and 11, Er is similar for the initial state and the monotonically deformed material in the cross and longitudinal section. Furthermore, no influence of hc on Er was observed considering scatter shown in Fig. 11. Thus, potential pile-up or sink-in effects are marginal so that the investigations in in the present are not relevantly affected.

$$\frac{1}{E_r}=\frac{1-\nu^2}{E}+\frac{1-\nu_i^2}{E_i} \qquad \text{(Eq. 5)}$$

The dependence of H on hc can be explained considering the model developed by Nix and Gao [24]: The measured H depends significantly on the dislocation density ρ. The dislocations can be divided into geometrically necessary and statistically distributed dislocations. Considering the numerous studies on the uniaxial, quasi-static hardening of TWIP steels, summarised by De Cooman [14] and Bouaziz [15], the dislocation density increases in addition to the twin density when TWIP steels are deformed. The difference between the TWIP steel in its initial state and after uniaxial deformation before indentation can be considered in the context of Nix and Gao's model [24] by attributing a higher density of statistically stored dislocations ρs for the uniaxially deformed material compared to the initial state. Furthermore, Nix and Gao's model [24] does not take the twin density into account, which is why this the role of twinning is discussed in the following paragraph separately. According to Nix and Gao [24], ρs remains approximately constant during nanoindentation, whereas ρg decreases as a function of hc. For $\varepsilon t \geq 45$ %, H decreases only insignificantly with increasing hc. Consequently, it can be assumed that $\rho s \gg \rho g$, so that the influence of ρg on H is negligible. Furthermore, a possible maximum of dislocation density could be reached for $\varepsilon t \geq 45$ % due to the indent's ρg. For $\varepsilon t < 45$ %, H decreases significantly with increasing hc, which can be explained by a lower ρs compared to $\varepsilon t \geq 45$ %. As a result, the decreasing ρg with increasing hc influences H. On top of that, the influence of ρg on H is greater for smaller εt and therefore, the increase in H with increasing εt is small compared to hardening observed in the monotonic stress-strain curve (Fig. 6). With increasing εt, this phenomenon declines as the ratio of $\rho g/\rho$ becomes smaller.

According to the model from Nix and Gao, the relation between H and h is given by Eq. (3)which can be transferred into Eq. (6)indicating a linear relation between H2 and 1/h.

$$H^2 = H_0^2 + h^* H_0^2 \frac{1}{h} \qquad \text{(Eq. 6)}$$

To evaluate the accordance of the TWIP steel's mechanical behaviour during nanoindentation with Eqs. (3) and (4), the H2-1/h curves are shown in Fig. 20. For $\varepsilon t \leq 30$ %, H2 increases linearly with increasing 1/h. For $\varepsilon t = 45$ %, a linear trend occurs for $10 \leq 1/h \leq 20$ whereas H is constant for $h < 10$ which can be explained by dislocation density saturation characterised by significantly lower ρg compared to ρs. Consistently, H2 is approximately constant in case of $\varepsilon t \geq 60$ %, too. As the H2-1/h curves agree with the prediction expressed in Eq. (4) for $\varepsilon t \leq 30$ %, either indentation does not result in twinning or hardening due to

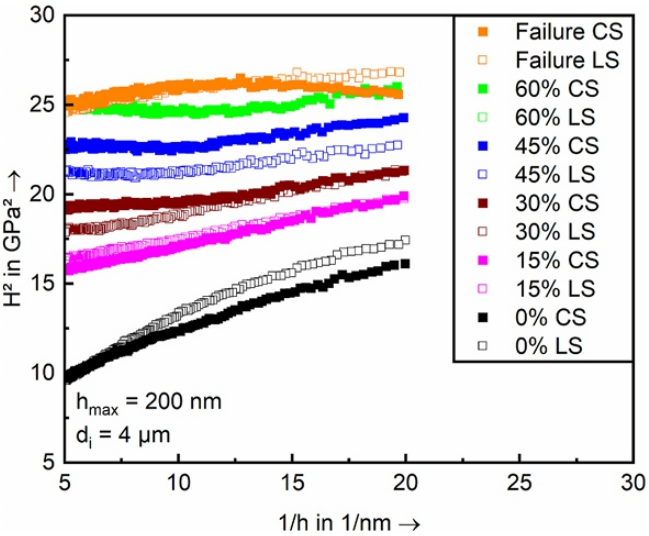

Fig. 20.H2 as a function of 1/h for verification of the agreement with the model from Nix and Gao [24].

twinning fulfils Eq. 4, too. Shang et al. [31] showed that the twin formation during nanoindentation of high manganese TWIP steel depends on the grain orientation while formation of dislocation structures occurs independently of the grain orientation. Considering the large number of indents summarised in Fig. 20, it is reasonable to assume that twinning occurred in some, but not necessarily all indentions. However, the H2-1/h are in good accordance with Eq. (4), which relies on a model that is solely based on dislocations. This suggests a minor contribution of twin boundaries to hardening through the reduction of the mean free path of dislocations in contrast to a major contribution of dislocation density to hardening of TWIP steel which is in accordance with the work of Liang et al. [35] and the literature review of De Cooman et al. [14], both on the monotonic hardening of TWIP steel.

In accordance with the CSM measurements on uniaxially deformed material, the H-ds curves shown in Fig. 14illustrate the necessity to considerate hmax when interpreting milling-induced hardness gradients as well. On the one hand, smaller hmax enable smaller di without influencing neighbouring indents, so that the hardness can be measured closer to the surface, resulting in larger maximum H values in the cross- section according to Fig. 16. On the other hand, H of softer materials conditions increases more than in case of harder material conditions with decreasing hmax due to the indentation size effect, resulting in smaller H differences for smaller hmax. This leads to a detection of the transition zone from the base material to the hardened layer at shallower depths in case of smaller hmax, resulting to an underestimation of the depth of the material volume hardened by milling.

This phenomenon provides further insights regarding the hardening behaviour during milling: Despite different stress states during deformation, the near-surface material volume hardened by milling exhibits a similar tendency regarding the H-hc-curves as the uniaxially deformed material does. A comparison of Figs. 8 and 14b) reveals that in both cases, areas of higher H show a smaller decrease of H as a function of hc than in areas with smaller H. Consequently, the H-hc curves can be interpreted in such a way that H and the decrease of H as a function of hc qualitatively reflects the amount of plastic deformation in the material volume. Thus, a higher H and a greater decrease in the H-hc curves qualitatively reveals stronger deformed material. Considering the work of Nix and Gao [24] in this context, higher milling induced H is a consequence of higher ρ. Thus, the H-hc curves enable qualitative comparison of ρ in different material volumes. Furthermore, the unknown deformation degree in the near surface material volume after milling can be qualitatively characterised and comparison to the uniaxially deformed material allows quantitative estimations of local plastic strains considering the relation between H and quasi-static σ shown in Fig. 20.

As hmax should not be reduced below 100 nm to guarantee a sufficient sensitivity of H for characterization of differently deformed material, a reduction of the ratio di/hmax is of interest to decrease di and thus increase the resolution in ds. A priori, an increase of H is likely if di/ h_{max} is such that the material deformed during successive indentation is partially overlapping. However, the differences in the H-ds curves for the investigated di/h_{max} ratios of 10, 15 and 20 shown in Fig. 16are within the hardness scatter, so that they cannot be clearly attributed to the decrease of di/h_{max} ratio. Hence, a reduction of di/h_{max} to a value of 10 is reasonable in accordance with the results of Sudharshan et al. [28].

The previously discussed results were established at cross sections transverse to the feed direction, but an examination of the longitudinal section is of interest due to the intermittent cutting during milling. The H-ds curves of longitudinal and cross sections in Fig. 17do not differ significantly which coincides with the examination of H at defined distances along the feed direction and at identical ds, shown in Fig. 17. Hence, no significant variation of H due to the cutting process was detected along the feed direction. Consequently, the discontinuous cutting process has no considerable effect on the hardness gradient in the material volume close to the surface. Accordingly, it is not relevant whether the hardness gradient is determined at the longitudinal or cross sections.

Through indentation with hmax = 25 nm it was shown that H de creases continuously from d = 1.25 μm on, so that the discontinuous grain size differences determined using the FIB technique do not lead to a local hardness drop at the transition from finer to coarser grains considering Fig. 19.

The discontinuous change in grain size determined using the FIB technique shown in Fig. 13 result according to Fig. 19 in a change in the gradient of the H-h c-curve, whereas no distinct hardness drop at the interface between nanocrystalline layer and the underlying microstructure is seen in Fig. 19. A sharp decrease in hardness could be expected considering exclusively the Hall-Petch relationship. Several authors (e. g. Refs. [3,7,36–41]) reported a nanocrystalline surface layer after maching of metallic materials. In the present work, the generation of these nanocrystalline structures is likely to be attributed to dynamic recovery or dynamic recrystallisation [39–41]. Both mechanisms result on the one hand in a decrease of dislocation density, which reduces hardness [39]. On the other hand, grain boundaries are generated which increases hardness [39]. Thus, the transition zone from the nanocrystalline surface layer to the coarser grained material volume is characterised by a change in the H-hc . -curve's gradient which can be explained by the onset of dynamic recovery or recrystallisation at a critical d s Furthermore, H decreases slightly in the nanocrystalline surface layer with increasing ds, revealing that the combination of ρ and grain boundaries results in H exceeding the biggest hardness in the coarser grained material volume with biggest slope of the H-d s ρ . However, the smaller curve in the nanocrystalline surface layer compared of that to the coarser grained material volume suggests that thermally activated reduction in ρ is more pronounced at shallower ds due to higher temperature [16]. Note that the existence of deformation twins in either region of the material volume modified by milling cannot simply be investigated using nanoindentation. An appropriate approach would be detailed transmission electron microscopy investigations that go beyond the present investigations.

Based on the previously discussed influences of h_{max} and di, h_{max} =100 nm, d I = 1 µ m and the observation of the cross section were identified as suitable for the comparative analysis of the hardness gradient in the material volume near the surface after milling. Using these parameters, the hardness gradient was determined after up milling, down milling, up milling and subsequent electrolytic polishing as well as in the rolling skin representing the initial state. According to Fig. 21, the hardness gradient after up and down milling is comparable despite the different kinematics during machining. In addition to the up and down milled surface morphologies, Fig. 21 shows a hardness increase in the

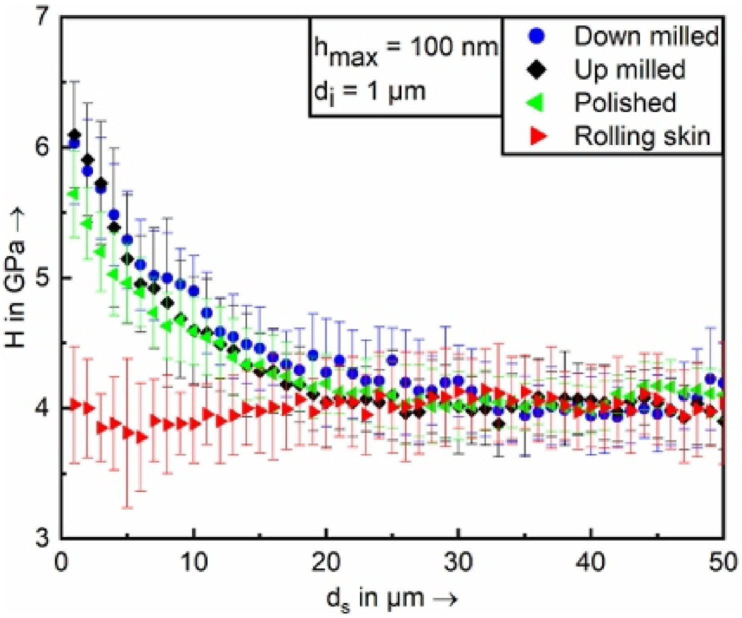

Fig. 21. Hardness gradient in the near surface regime after down and up milling, up milling and subsequent, electrolytical polishing as well as after rolling.

material volume near the surface despite electrolytic polishing. In the present case, material volume up to a depth of approx. 3 µ m was µ removed, so that the hardness-surface distance is shifted by approx. 3 µ m to smaller surface distances. Furthermore, the material volume close to the rolling skin has an insignificantly lower hardness compared to the base material according to Fig. 21. In this respect, the rolling process does not lead to a hardened surface layer.

The decreasing hardness for the milled surface with increasing ds , which asymptotically approaches the hardness of the base material according to Fig. 21 is consistent with work on surface morphologies established by milling [3,4] as well as turning [7,8,19,20]. However, Klein et al. [3] and Laamouri et al. [4] found differences between the near-surface material volumes produced by up and down milling regarding the maximum increase in hardness compared to the base material and the depth of the material volume hardened by milling, which was not observed in the present work. On top of that, the increase in hardness compared to the base material of approximately 50 % is significantly greater than the increase in hardness of approx. 10 % in the case of up milling and 5 % of down milling of the high-manganese steel HSD®600 measured by Klein et al. [3] normal to the surface with F_{max} = 1000 mN. Furthermore, the depth of the material volume modified by milling is with 54 µm considerably bigger in the work of Klein et al. [1]. As the depth of the elastic-plastically deformed material volume during indentation testing with F_{max} =1000 mN was estimated by Klein et al. m, the hardness Klein et al. [3] measured at the surface results from a material volume exhibiting a pronounced hardness gradient. This explains the lower hardness increase through milling compared with the results from the present work.

The hardness increases of 75 % determined by Laamouri et al. [4] after up milling and 45 % after down milling of the high-alloy steel X160CrMoV12 is closer to the hardness increase determined in the present study than the results of Klein et al. [3]. The depth of the up milled layer was tremendously bigger in the work of Laamouri et al. [4] facilitating the determination of the hardness slope through higher indentation forces and depth. Furthermore, the hardness increase of approximately 100 % determined by Boemke et al. [7], Skorupski et al. [8] and Mayer et al. [19] after turning with cryogenic cooling of AISI 347 and AISI 904L is greater than the hardness increase determined in the present work. With 150 μ m–400 μ m [5,7,16], the depth of the material volume hardened by turning was also greater than the transition depth from the hardened layer to the base material determined in the present study. Although a slight underestimation of the depth is possible in the present work due to the indentation size effect, the differences to the discussed studies [3,4,7,8,19] are too large to be based on this phenomenon. Overall, the hardness gradients in the near-surface material volume after milling have not been investigated enough to be able to explain differences conclusively when influencing factors such as mechanical properties of the machined material and cutting parameters are excluded.

5. Conclusion

The hardness increase due to uniaxial, quasi-static deformation was determined for six different elongations. In addition, CSM was used to show that the indentation size effect influences the measured hardness significantly. With increasing deformation and hardness, the decrease in hardness as a function of contact depth becomes smaller. This can be explained by an increase in dislocation density during quasi-static deformation, revealing that CSM measurements provide indications of the deformation-induced increase in dislocation density, which can be useful for the analysis of highly localized deformation fields, e.g. after milling. The indentation size effect was also studied in the context of milling- induced hardness gradient characterization. Smaller h_{max} enable a more detailed resolution of the hardness gradient, a closer positioning to the surface and thus higher maximum hardness values. In contrast, the indentation size effect results in smaller hardness differences between different material conditions, leading to an underestimation of the hardened zone with decreasing h_{max} . A suitable compromise between sensitivity and resolution was identified as $h_{c\,max} = 100$ nm. These results were further analysed using CSM, analogous to the quasi-static, uniaxially deformed material conditions. In agreement with the quasi- statically deformed material conditions, a greater hardness in the zone affected by milling correlates with a lower decrease in H as a function of h . In this respect, the increase in hardness in the milled zone can also be attributed to an increased dislocation density compared to the base material.

For further improvement of the hardness to surface distance curve's resolution, it was tested whether the ratio di/hmax could be reduced to 10. The difference in the H-hc curves for di/ hmax =20, di/hmax =15 and di/hmax =10 is so small that di/hmax =10 was identified as suitable in accordance with the literature.

As the surface generation during milling is generated by interrupted cuts, the hardness gradient was analysed in a longitudinal section along the feed direction. No difference in hardness could be identified along the feed direction at defined surface distances, i.e., there is no hardness gradient in the feed direction that goes beyond the scatter of the measurement data. Furthermore, the locally discontinuous transition from the fine- grained layer, which comprises the first 1–2 μ m of the near-surface material volume established by milling, to the significantly coarser- grained material volume was investigated. In the transition zone, an increase in the H-d s curve's slope is observed, in contrast to the decreasing slope outside this material volume. This suggests a reduction in dislocation density within the nanocrystalline surface layer, likely due to thermally activated mechanisms leading to the fine-grained material volume.

Finally, the hardness-depth curves in the near-surface volumes produced by up and down milling were compared, and no significant differences were identified. The maximum increase in hardness at a surface distance of 1 μ m is approx. 50 % and the depth of the material volume modified by milling is approx. 20 μ m. The hardness decreases degressively with increasing surface distance, resulting in an asymptotic approach of the base material's hardness. After electrolytic polishing, the hardness-surface distance curve is shifted approximately 3 μ m towards smaller surface distances compared to that after up milling, revealing that not the whole hardened volume was removed and conf irming the presented method as reliable for the characterization of different milling induced hardened material volumes.

CRediT authorship contribution statement

S. Wolke: Writing – review & editing, Writing – original draft, Visualization, Validation, Methodology, Investigation, Formal analysis, Data curation, Conceptualization. **M. Smaga:** Validation, Supervision, Resources, Project administration, Funding acquisition, Conceptualization. **T. Beck:** Validation, Supervision, Software, Resources, Project administration, Funding acquisition, Conceptualization.

Declaration of competing interest

The authors declare that they have no known competing financial interests or personal relationships that could have appeared to influence the work reported in this paper.

Acknowledgement

This work was funded by the Deutsche Forschungsgemeinschaft (DFG, German Research Foundation) – project number 172116086 – SFB 926. The authors thank thyssenkrupp Hohenlimburg GmbH for providing the TWIP steel 1.7401.

Data availability

Data will be made available on request.

References

[1] DIN Deutsches Institut für Normung e.V., ISO 25178-2:2021: Geometrical Product Specifications (GPS) – Surface Texture: Areal – Part 2: Terms, Definitions and Surface Texture Parameters.

[2] W.C. Oliver, G.M. Pharr, An improved technique for determining hardness and elastic modulus using load and displacement sensing indentation experiments, J. Mater. Res. 7 (1992) 1564–1583, https://doi.org/10.1557/JMR.1992.1564.

[3] M.W. Klein, B. Blinn, M. Smaga, T. Beck, High cycle fatigue behavior of high-Mn TWIP steel with different surface morphologies, Int. J. Fatig. 134 (2020) 105499, https://doi.org/10.1016/j.ijfatigue.2020.105499.

[4] A. Laamouri, F. Ghanem, C. Braham, H. Sidhom, Influences of up-milling and down-milling on surface integrity and fatigue strength of X160CrMoV12 steel, Int. J. Adv. Manuf. Technol. 105 (2019) 1209–1228, https://doi.org/10.1007/s00170- 019-04280-2.

[5] C. Yao, D. Wu, L. Ma, L. Tan, Z. Zhou, J. Zhang, Surface integrity evolution and fatigue evaluation after milling mode, shot-peening and polishing mode for Tb6 titanium alloy, Appl. Surf. Sci. 387 (2016) 1257–1264, https://doi.org/10.1016/j. apsusc.2016.06.162.

[6] M. Smaga, T. Beck, M. Kopnarski, R. Merz, K.M. de Payrebrune, S. Wolke, Influence of Surface Morphology on Fatigue and Tribological Behavior of TRIP/TWIP Steels 289–312. https://doi.org/10.1007/978-3-031-35575-2_12.

[7] A. Boemke, Einfluss kryogen gedrehter Randschichten auf das Ermüdungsverhalten des metastabilen austenitischen Stahls X6CrNiNb1810 und des stabilen austenitischen Stahls X1NiCrMoCu25205 bis in den VHCF-Bereich. PhD thesis.

[8] R. Skorupski, M. Smaga, D. Eifler, Influence of surface morphology on the fatigue behavior of metastable austenitic steel, AMR (Adv. Magn. Reson.) 891–892 (2014) 464–469. https://doi.org/10.4028/www.scientific.net/AMR.891-892.464.

[9] T. Oevermann, T. Wegener, T. Niendorf, On the evolution of residual stresses, microstructure and cyclic performance of high-manganese austenitic TWIP-steel after deep rolling, Metals 9 (2019) 825, https://doi.org/10.3390/met9080825.

[10] M. Smaga, R. Skorupski, P. Mayer, B. Kirsch, J.C. Aurich, I. Raid, J. Seewig, J. Man, D. Eifler, T. Beck, Influence of surface morphology on fatigue behavior of metastable austenitic stainless steel AISI 347 at ambient temperature and 300◦C, Procedia Struct. Integr. 5 (2017) 989–996, https://doi.org/10.1016/j. prostr.2017.07.150.

[11] J.C. Aurich, H. Hasse (Eds.), Component Surfaces: Manufacturing-Morphology- Property Relationships, Springer, Cham, 2024.

[12] M. Kaladhar, K.V. Subbaiah, C.S. Rao, Machining of austenitic stainless steels - a review, IJMMM 12 (2012) 178, https://doi.org/10.1504/IJMMM.2012.048564.

[13] D. Pal, S. Basu, Hot machining of austenitic manganese steel by shaping, Int. J. Mach. Tool Des. Res. 11 (1971) 45–61, https://doi.org/10.1016/0020-7357(71) 90046-1.

[14] B.C. de Cooman, Y. Estrin, S.K. Kim, Twinning-induced plasticity (TWIP) steels, Acta Mater. 142 (2018) 283–362, https://doi.org/10.1016/j.actamat.2017.06.046.

[15] O. Bouaziz, S. Allain, C.P. Scott, P. Cugy, D. Barbier, High manganese austenitic twinning induced plasticity steels: a review of the microstructure properties relationships, Curr. Opin. Solid State Mater. Sci. 15 (2011) 141–168, https://doi. org/10.1016/j.cossms.2011.04.002.

[16] S. Chauhan, R. Trehan, R.P. Singh, State of the art in finite element approaches for milling process: a review, Adv. Manuf. 11 (2023) 708–751, https://doi.org/ 10.1007/s40436-022-00417-x.

[17] H.S. Kramer, P. Starke, M. Klein, D. Eifler, Cyclic hardness test PHYBALCHT – short-time procedure to evaluate fatigue properties of metallic materials, Int. J. Fatig. 63 (2014) 78–84, https://doi.org/10.1016/j.ijfatigue.2014.01.009.

[18] K.L. Johnson, The correlation of indentation experiments, J. Mech. Phys. Solid. 18 (1970) 115–126, https://doi.org/10.1016/0022-5096(70)90029-3.

[19] P. Mayer, R. Skorupski, M. Smaga, D. Eifler, J.C. Aurich, Deformation induced surface hardening when turning metastable austenitic steel AISI 347 with different cryogenic cooling strategies, Procedia CIRP 14 (2014) 101–106, https://doi.org/ 10.1016/j.procir.2014.03.097.

[20] Y. Guo, J. Sahni, A comparative study of hard turned and cylindrically ground white layers, Int. J. Mach. Tool Manufact. 44 (2004) 135–145, https://doi.org/ 10.1016/j.ijmachtools.2003.10.009.

[21] A. Javidi, U. Rieger, W. Eichlseder, The effect of machining on the surface integrity and fatigue life, Int. J. Fatig. 30 (2008) 2050–2055, https://doi.org/10.1016/j. ijfatigue.2008.01.005.

[22] G.M. Pharr, E.G. Herbert, Y. Gao, The indentation size effect: a critical examination of experimental observations and mechanistic interpretations, Annu. Rev. Mater. Res. 40 (2010) 271–292, https://doi.org/10.1146/annurev-matsci-070909- 104456.

[23] G. Voyiadjis, M. Yaghoobi, Review of nanoindentation size effect: experiments and atomistic simulation, Crystals 7 (2017) 321, https://doi.org/10.3390/ cryst7100321.

[24] W.D. Nix, H. Gao, Indentation size effects in crystalline materials: a law for strain gradient plasticity, J. Mech. Phys. Solid. 46 (1998) 411–425, https://doi.org/ 10.1016/S0022-5096(97)00086-0.

[25] X. Li, B. Bhushan, A review of nanoindentation continuous stiffness measurement technique and its applications, Mater. Char. 48 (2002) 11–36, https://doi.org/ 10.1016/S1044-5803(02)00192-4.

[26] S. Curtze, V.-T. Kuokkala, A. Oikari, J. Talonen, H. H¨anninen, Thermodynamic modeling of the stacking fault energy of austenitic steels, Acta Mater. 59 (2011) 1068–1076, https://doi.org/10.1016/j.actamat.2010.10.037.

[27] DIN Deutsches Institut für Normung e.V., DIN EN ISO 6892-1:2014: Metallic Materials - Tensile Testing - Part 1: Method of Test at Room Temperature (ISO/DIS 6892-1:2014), accessed 2014.

[28] P. Sudharshan Phani, W.C. Oliver, A critical assessment of the effect of indentation spacing on the measurement of hardness and modulus using instrumented indentation testing, Mater. Des. 164 (2019) 107563, https://doi.org/10.1016/j. matdes.2018.107563.

[29] K. Durst, B. Backes, O. Franke, M. G¨oken, Indentation size effect in metallic materials: modeling strength from pop-in to macroscopic hardness using geometrically necessary dislocations, Acta Mater. 54 (2006) 2547–2555, https:// doi.org/10.1016/j.actamat.2006.01.036.

[30] K. Durst, B. Backes, M. G¨ oken, Indentation size effect in metallic materials: correcting for the size of the plastic zone, Scr. Mater. 52 (2005) 1093–1097, https://doi.org/10.1016/j.scriptamat.2005.02.009.

[31] X.K. Shang, S. Pan, Q.W. Guan, B.B. He, Orientation dependent twinning behavior in a twinning-induced plasticity steel investigated by nanoindentation, Met. Mater. Int. 28 (2022) 2874–2883, https://doi.org/10.1007/s12540-022-01180-1.

[32] J. Kim, B.C. de Cooman, On the stacking fault energy of Fe-18 Pct Mn-0.6 Pct C-1.5 Pct Al twinning-induced plasticity steel, Metall. Mater. Trans. A 42 (2011) 932–936, https://doi.org/10.1007/s11661-011-0610-6.

[33] M.W. Klein, M. Smaga, T. Beck, Influence of the surface morphology on the cyclic deformation behavior of HSD® 600 steel, MATEC Web Conf. 165 (2018) 6010, https://doi.org/10.1051/matecconf/201816506010.

[34] D.T. Pierce, K. Nowag, A. Montagne, J.A. Jim´ enez, J.E. Wittig, R. Ghisleni, Single crystal elastic constants of high-manganese transformation- and twinning-induced plasticity steels determined by a new method utilizing nanoindentation, Mater. Sci. Eng., A 578 (2013) 134–139, https://doi.org/10.1016/j.msea.2013.04.049.

[35] Z.Y. Liang, Y.Z. Li, M.X. Huang, The respective hardening contributions of dislocations and twins to the flow stress of a twinning-induced plasticity steel, Scr. Mater. 112 (2016) 28–31, https://doi.org/10.1016/j.scriptamat.2015.09.003.

[36] J. Barry, G. Byrne, TEM study on the surface white layer in two turned hardened steels, Mater. Sci. Eng., A 325 (2002) 356–364, https://doi.org/10.1016/S0921- 5093(01)01447-2.

[37] A. Ramesh, S.N. Melkote, L.F. Allard, L. Riester, T.R. Watkins, Analysis of white layers formed in hard turning of AISI 52100 steel, Mater. Sci. Eng., A 390 (2005) 88–97, https://doi.org/10.1016/j.msea.2004.08.052.

[38] V. Schulze, F. Zanger, F. Ambrosy, Quantitative microstructural analysis of nanocrystalline surface layer induced by a modified cutting process, AMR (Adv. Magn. Reson.) 769 (2013) 109–115. https://doi.org/10.4028/www.scientific. net/AMR.769.109.

[39] S. Buchkremer, F. Klocke, Modeling nanostructural surface modifications in metal cutting by an approach of thermodynamic irreversibility: derivation and experimental validation, Continuum Mech. Therm. 29 (2017) 271–289, https:// doi.org/10.1007/s00161-016-0533-y.

[40] S. Buchkremer, F. Klocke, B. D¨ obbeler, M. Abouridouane, M. Meurer, Thermodynamics-based interpretation of white layer formation in metal cutting, Procedia CIRP 58 (2017) 370–374, https://doi.org/10.1016/j.procir.2017.03.328.

[41] H. Liu, X. Xu, J. Zhang, Z. Liu, Y. He, W. Zhao, Z. Liu, The state of the art for numerical simulations of the effect of the microstructure and its evolution in the metal-cutting processes, Int. J. Mach. Tool Manufact. 177 (2022) 103890, https:// doi.org/10.1016/j.ijmachtools.2022.103890.

ISSN: 1757-899X

From a notch to a crack: Monitoring crack initiation from a notch through cyclic bending of microscale cantilevers

Ali Kaveh 1, M.H. Shahini 1, Xiaoman Zhang 1 , Wangwang Xu, Parisa Z. Firouzabadi, Bin Zhang, W.J. Meng*
Department of Mechanical and Industrial Engineering, Louisiana State University,
Baton Rouge, LA, 70803, USA

ABSTRACT

Cyclic bending is conducted on pre-notched microscale cantilevers fabricated from Si-modified Inconel 939 and Inconel 718 alloy specimens made by laser powder bed fusion additive manufacturing. Under a fixed cyclic loading condition, we show that this test can be used to determine the number of loading cycles needed to initiate an actual fatigue crack from a notch fabricated by focused ion beam milling. Further, we show that this threshold cycle number to crack initiation (*Nth*) obeys Weibull statistics when repeat tests are conducted on multiple cantilevers with notches fabricated under nominally the same conditions. The present microscale testing protocol allows a more detailed examination of the various factors influencing fatigue crack initiation from notches. As an example, the dependence of *Nth* on loading frequency is measured for Inconel 718 alloy specimens over a frequency range wider than what is possible from macroscale testing.

1. Introduction

It has long been known that measurements of fatigue life exhibit marked variability and should be represented in statistical terms [1]. Fatigue stress – life (S-N) data obtained from widely varying mechanical loading configurations under fixed cyclic loading conditions have been shown to obey Weibull statistics, examples include bending fatigue [2], rolling contact fatigue [3], alternating torsion fatigue [4], and tension-tension fatigue [5].

It is also well accepted that total fatigue life consists of two phases: the fatigue crack initiation (FCI) phase followed by the fatigue crack growth (FCG) phase until eventual specimen failure [6,7]. While fatigue cracks are recognized to start usually at free surfaces in unnotched and structurally homogeneous specimens [7], defects within engineering materials are often observed to dominate crack initiation, e.g., large pores in aluminum castings [5,8]. In alloy specimens fabricated by laser powder bed fusion additive manufacturing (L-PBF AM), the common observation from a large body of fatigue testing has been that fatigue failure most often occurs through crack initiation from defects generated during the printing process [9], e.g., lack-of-fusion pores [9,10].

To date, measurements of FCG have predominantly been carried out using specimens with characteristic sizes in the macroscopic scale (>1 cm), following well documented procedures [11]. The same statement applies to FCG measurements performed on L-PBF AM alloy specimens [12]. In such macroscale specimens, conventional machining techniques, such as electric discharge machining, mechanical milling or broaching, are used to fabricate notches with large tip radii ρ specification: ρ < 75 μ (example m [11]). As notches with such large tip radii do not constitute actual cracks, such test procedures dictate that "pre– cracking" is to occur before data are recorded to ensure that a sharpened fatigue crack is present as the test starts. While this is aimed at eliminating any influence of the machined notch on subsequent FCG data [11], this act of pre-cracking foregoes obtaining any information on the transition from a notch to an actual crack. A similar comment can be made about S-N measurements on unnotched specimens at fixed loading conditions or stress levels [13]: only the total number of loading cycles until specimen failure is recorded in such tests, thus the test again offers no information on the number of loading cycles needed to initiate a crack, whose subsequent propagation results in specimen failure. In the present literature regarding fatigue testing of specimens processed by L-PBF AM, it is recognized that a clear distinction between the crack initiation phase and crack growth phase is often not made in the data acquired [14].

A prevalent narrative in the present AM literature professes that fatigue strength and life of AM materials are dominated by the defect of the largest size within the printed material volume [15]. Such an extreme value statistics approach [15] is based on the rationale that the process of FCI from a defect is so easy that it can be ignored, and consequently the largest defect present can be regarded as the largest crack present [16,17]. In reality, even though defects generated during AM processing can have rather sharp features, e.g., with the minimum radius of curvature of the lack-of-fusion pores in L-PBF AM materials in the range of tens of nm [10], they are blunt from an atomistic perspective, being tens to hundreds of atomic planes wide. The process of fatigue crack initiation from a notch is a process of affecting additional separation of atomic planes from such atomistically blunt features, and measurements capable of quantifying such an FCI process can thus be used to better gauge the various factors influencing this process. One of such factors is the loading frequency.

Frequencies of cyclic loading carried out on macro-sized specimens with hydraulically driven machines are typically limited to below 100 Hz [18]. Ultrasonically driven fatigue testing techniques have been developed more recently, with a typical loading frequency around 20 kHz [19]. It is recognized that engineering materials are often subjected to loading at variable stress amplitudes and frequencies in application settings [20]. It has also been reported previously that changing the loading frequency from <100 Hz to 20 kHz can have a significant effect on the measured total fatigue life as well as the fatigue strength [8,21].

Therefore, it can reasonably be asked whether loading frequency would influence the process of crack initiation from a notch of a given geometry. Concrete results in answering this question may provide clues to a better understanding of the physics controlling FCI from notches under cyclic loading. In this paper, we report the results of cyclic bending tests performed on pre-notched microscale cantilevers fabricated from Si-modified Inconel 939 and Inconel 718 alloy specimens made by L-PBF AM. We show that, in contrast to macroscale S-N and FCG measurements, cyclic bending of pre-notched micro cantilevers is sensitive to crack initiation from the notch and can offer a quantitative measure for it. Repeat tests under a fixed loading condition on separate cantilevers, with pre- notches fabricated by focused ion beam (FIB) milling under the same beam parameters, show that the number of loading cycles to initiate an actual fatigue crack can be measured, and that this threshold cycle number (Nth) obeys Weibull statistics. Weibull statistics can in turn be used to better quantify the influence of loading frequency on FCI from a notch.

2. Methods

Morphological, structural, compositional characterization and nano/ micro scale machining were carried out using X-ray, electron, and ion beam methods. X-ray diffraction (XRD) was performed on a PANalytical Empyrean system with Cu Kα radiation. Symmetric θ/2θ scans were conducted in the angular range of 20–120◦ 2θ. Milling with Xe+FIB, scanning electron microscopy (SEM), X-ray energy dispersive spectroscopy (EDS), and electron backscatter diffraction (EBSD) measurements were carried out on a Xe+plasma focused ion beam/scanning electron microscopy instrument (PFIB/SEM, ThermoFisher Helios G4) housing an Oxford EDS/EBSD system, an EasyLift® nanoprobe for specimen lift- out, and a MultiChem® gas injection system for ion beam catalyzed, spatially selective deposition of W. EDS mapping and EBSD mapping were conducted at electron beam voltage and current of 20 kV and 1.6 nA, respectively.

Two different alloy specimens processed by L-PBF AM were used in the present study. First, a custom-built selective laser melting machine [22,23] was used to process mixtures of commercial gas-atomized Inconel 939 powders (Carpenter Additive, USA) with 3 wt% of added commercial Si particles (99.5 %+, Alfa Aesar, USA) into Si-modified Inconel 939 (IN939-Si) alloy specimens. As-printed IN939-Si specimens were disk-shaped with dimensions of 10 mm ×10 mm ×6 mm. As-printed disks were mechanically polished so that the normal of the flat top and bottom disk surfaces was parallel to the AM build direction (BD). Further details on the L-PBF AM processing parameters for the IN939-Si specimens were reported elsewhere [24]. Second, L-PBF AM Inconel 718 (IN718) alloy specimens were obtained from a previous benchmark study in which different geometrical shapes were built on top of an IN718 base plate, with design specifications following standard guidelines for AM parts [25]. As-printed IN718 shapes received a stress relieving heat treatment at 1066 ◦C for 90 min followed by a slow furnace cool, and no other known heat treatment [26]. Further details on the IN718 specimen fabrication process were also given in Ref. 26. Out of the various shapes built by AM in the benchmark study, the In718 specimens used in the present experiments were extracted from the "Simulated Inducer Freeform Surface" shape. The simulated inducer had a complex spiraling shape built on a flat base several mm in thickness. Flat IN718 disks were mechanically cut from this flat base region and polished into disks, with the normal of the flat top and bottom disk surfaces parallel to the AM BD. The benchmark study documented in Ref. 26 involved IN718 parts fabricated by 16 vendors, and it was unknown to the present investigators which vendor fabricated the simulated inducer part used in this study.

IN939-Si and IN718 disks were mechanically polished to possess smooth and parallel top and bottom surfaces and 90◦edges with respect to the top and bottom surfaces. The PFIB/SEM instrument was employed to fabricate one-end-attached micro cantilever beams onto the mechanically polished disks by sequential Xe+FIB milling of the disk edge region from the top surface and the front side surface, as illustrated in Fig. 1(a). All cantilevers were aligned with disk edges, with overall dimensions of ~100 μm ×~25 μm ×~25 μm. Procedures for FIB milling were applied consistently for all cantilevers: the Xe+ion beam voltage was held at 30 kV while the beam current decreased in steps, from 2.5 μA to 1 μA, 0.20 μA, 60 nA, and 4 nA. A pre-notch was milled onto the cantilever top surface at ~25 μm from the bulk attachment for all cantilevers. The pre-notch depth was about 1/3 of the cantilever beam thickness (~8 μm). The pre-notch was milled using the line cut mode of the PFIB instrument, with the Xe+ion beam parameters set at 30 kV and 4 nA. Right after cantilever fabrication, dimension measurements were conducted to record the cantilever thickness t, width B, length l, pre- notch depth ao, and distance between the notch tip to the cantilever bottom t-ao (Fig. 1(b)). The load length lL, i.e., the distance between the actuator contact point on the cantilever and the pre-notch, was measured prior to the start of each cyclic bending test (Fig. 1(b)).

Cyclic bending of pre-notched cantilevers was performed using an instrumented uniaxial nanomechanical actuator (FemtoTools NMT-04) within an SEM (FEI Quanta3D FEG). As shown in Fig. 1(b), the shape of the Si actuator tip was modified by FIB milling to fit the cantilever dimensions. One group of cantilevers were fabricated from as-deposited L-PBF AM IN939-Si disk following the protocol described above. Five groups of cantilevers were fabricated from as-deposited L-PBF AM IN718 disk following the same protocol. The IN939-Si cantilever group was tested under cyclic bending at a fixed loading frequency f of 100 Hz and fixed maximum/minimum bending forces (F_{max}/F_{min}) of

49500 µN and 4500 µN, and thus at a fixed load ratio $R = F_{min}/F_{max}$ of 1/11. The five groups of IN718 cantilevers were tested under cyclic bending at five different f values of 40, 100, 400, 500, and 600 Hz, all under the same fixed Fmax and F_{min} of 80000 µN and 50000 µN, and thus at a fixed R value of 5/8. The Fmax and R values used for testing IN939-Si and IN718 cantilevers were determined experimentally through separate runs, such that cantilever failure was neither premature (e.g., failure within a few tens of loading cycles) nor overly extended (e.g., no failure in several million cycles). The increased F_{max} and R values for IN718 testing as compared to those for IN939-Si testing reflect the increased difficulty in failing IN718 cantilevers as compared to IN939-Si cantilevers.

Load and actuator displacement were measured continuously during cyclic bending tests. Before running an actual test, the actuator system stiffness was measured by performing a compression test with the same actuator on the surface of the disk bulk, away from the cantilever. This system stiffness was subtracted from the test data to obtain the true actuator displacement. Fig. 2(a), (b), and 2(c) show, respectively, typical data segments acquired during cyclic bending of pre-notched In718 cantilevers at f =100, 400, and 600 Hz. The corresponding load- displacement data are shown in Fig. 2(d), (e), and 2(f), respectively,

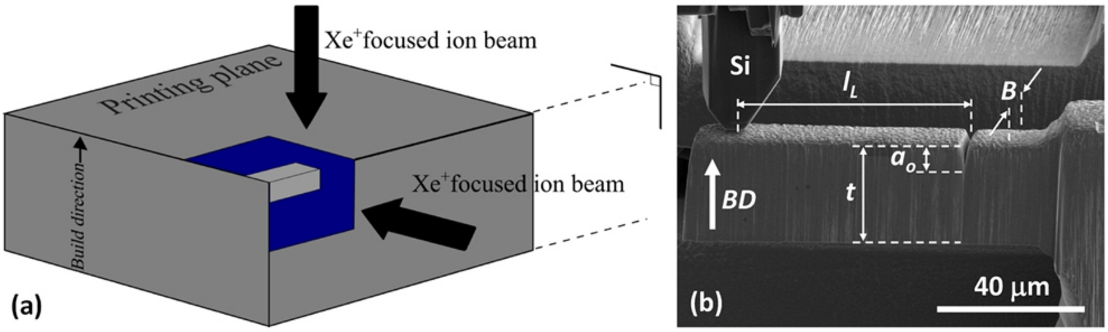

Fig. 1. (a) A schematic illustration of the Xe + FIB milling setup for micro cantilever fabrication; (b) a typical IN939-Si pre-notched micro cantilever prior to cyclic bending within an SEM. The cantilever long axis is oriented perpendicular to the L-PBF AM build direction (BD)

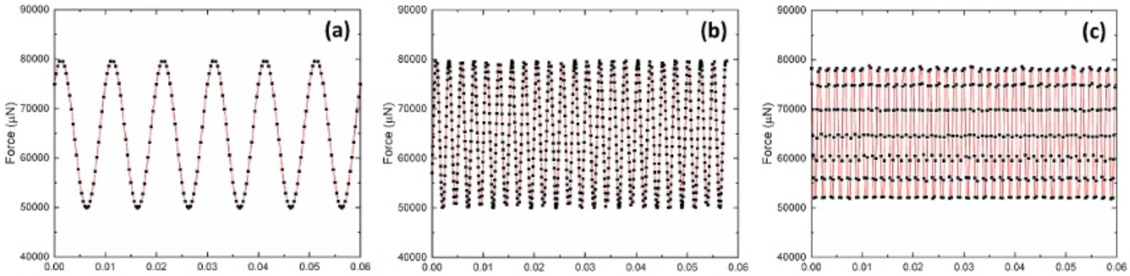

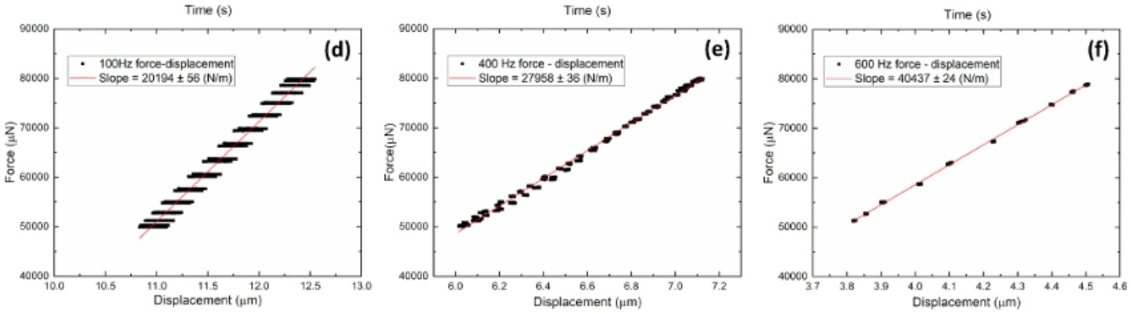

Fig. 2. Load and frequency control in cyclic bending experiments: (a/b/c) typical bending load force vs. time at frequencies of 100, 400, and 600 Hz; (d/e/f) corresponding load vs. displacement obtained from the dataset shown in (a/b/c). The solid red lines in (d/e/f) are linear least squares fits to the load vs. displacement data, from which the bending stiffness is obtained. (For interpretation of the references to colour in this figure legend, the reader is referred to the Web version of this article.)

from which the cantilever bending stiffness is obtained. The same level of frequency and force control as demonstrated in Fig. 2 was achieved in all cantilever bending tests. Prior to the actual cyclic bending test conducted on a micro cantilever, the initial bending stiffness of the cantilever was recorded for a short duration of less than 1 s. This measured initial stiffness was used to set a criterion for test stopping: i.e., the test will stop when measured cantilever bending stiffness drops to a preset fraction of the initial stiffness.

To better characterize how a fatigue crack initiates from the pre- notch, we first quantify the geometry of the pre-notch in as-fabricated cantilevers by FIB milling. Destructive three-dimensional (3D) tomography of as-fabricated cantilevers was performed on the PFIB/SEM instrument using the “slice-and-view” technique, where the Xe + ion beam was employed for serial sectioning at a preset slice thickness and the electron beam was used for secondary electron imaging of the sectioning surface after each slice. A part of the as-fabricated cantilever containing the pre-notch was milled off from the attachment, lifted out using the EasyLift® nanoprobe following standard procedures, and attached to the edge of a Si wafer. The lifted-out and attached chunk was then flipped manually so that the pre-notch faced downward, away from the slicing Xe ion beam. A ~400 nm thick W layer was ion beam deposited onto the top left corner of the chunk. A fiducial mark was FIB milled into the W layer and served as the reference point for aligning the ion and electron beams during successive slicing operations. No additional protective coating was applied to the surface. The cantilever chunk was sliced using the Xe + ion beam at voltage and current of 30 kV and 4 nA, respectively. The slicing thickness was set to 700 nm, providing sufficient resolution for the analysis. SEM images were acquired in the immersion mode after each slice at beam voltage and current of 5 kV and 0.1 nA, respectively. Following the slice-and-view experiment, image processing and 3D reconstruction were conducted using the Avizo software (Avizo

3D 2021.1). Initially, all the acquired SEM images were manually aligned using the Align Slices tool. Segmentation of the notch (empty) and cantilever (solid) areas was then completed in the Segmentation Editor. Finally, the segmented images were compiled into a 3D model through Volume Rendering. In the 3D model built from low magnification images, each voxel measured 10 nm along the x- and y- axes and 700 nm along the z-axis. For the 3D model built from high magnification images, each voxel measured 1 nm along the x- and y-axes and 700 nm along the z-axis. To illustrate the initiation of fatigue crack from the pre-notch after mechanical loading, the same slice-and-view protocol was used to examine additional cantilevers after they have been cyclically loaded.

3. Results and discussion

The present authors have previously conducted quantitative FCG measurements on IN939-Si alloy specimens processed by L-PBF AM through cyclic bending of pre-notched micro cantilevers [27]. As shown in Fig. 1(b), one-end-attached pre-notched micro cantilevers fabricated from as-printed IN939-Si were fabricated via Xe + FIB milling (B ≈ t ≈25 μ m, ao~ t/3), with the cantilever long axis perpendicular to the AM BD. Cyclic bending within an SEM was executed at a fixed frequency f = 100 Hz and a fixed load ratio R = 1/11. Bending stiffness S was measured as a function of loading cycle N, converted into a measure of the fatigue crack length a vs. N through comparison with elastic FEA simulations, with the conversion confirmed through post-test microscopy of the fracture surface [27]. The mode I stress intensity factor KI associated with bending load F, crack length a, load length lL, and specimen dimensions B and t was calculated by taking results from a prior micro cantilever bending study [28],

$$K_I = \frac{F l_L}{B t^{3/2}} f(a / t), \tag{1}$$

and

$$f(a / t) = 77.608(a/t)^3 - 48.422(a/t)^2 + 24.184(a/t)^1 + 1.52. \tag{2}$$

This KI calculation was confirmed through comparison between calculated K values and measured bending compliance C as a function of a (K^2 vs. dC/da; C=1/S) [27].

Fig. 3 (a) shows the raw data for one typical IN939-Si cantilever cyclic bending measurement, plotted as bending stiffness S vs. the number of loading cycles N. The raw data are taken from the previous study described in Ref. 27. After converting the S – N data to crack length a vs. N, the crack growth rate da/dN is obtained by taking a numerical derivative of the a – N curve. Fig. 3(b) shows the corresponding crack growth curve, da/dN vs. ΔK with ΔK = K(F max) – K(F min). This crack growth curve exhibits characteristics similar to those observed from macroscale FCG measurements. Despite the small specimen size, both the threshold regime and the Paris-law regime of crack growth are evident, as highlighted respectively by the blue and red dashed lines, representing power law fits through the corresponding data segments. Data shown in Fig. 3(b) exhibit an extended subthreshold regime with da/dN values persisting around 10^{-3} µm/cycle or below. This is better illustrated in Fig. 3(c), where the same data is plotted as da/dN vs. N: da/dN values stay at 10^{-3} µm/cycle or below for ~5 × 10 4 cycles before a rapid and significant upturn is observed. It is noted that both positive and negative da/dN values are exhibited in the subthreshold regime shown in Fig. 3©. This is a result of taking numerical derivative on the raw a – N data, and the noisy a – N data reflect the fact that little crack growth occurs in this subthreshold regime. By fitting a linear function to the upturn portion of the da/dN vs. N data and extrapolating to da/dN = 0, a threshold number of loading cycles, N th, is obtained. That a threshold number of loading cycles, Nth, are needed for da/dN to in crease beyond the subthreshold regime (e.g., >2 × 10-3 µm/cycle) is clearly illustrated in Fig. 3(c) but not stated in Ref. 27. Further, the existence of Nth is born out of the cyclic bending measurements, notwithstanding the noisy measurement evidenced in Fig. 3©. Because da/dN – N curves exhibit a sharp and significant upturn at N th , while a – N curves varies more smoothly with N (compare Fig. 3(a) and (c)), it is

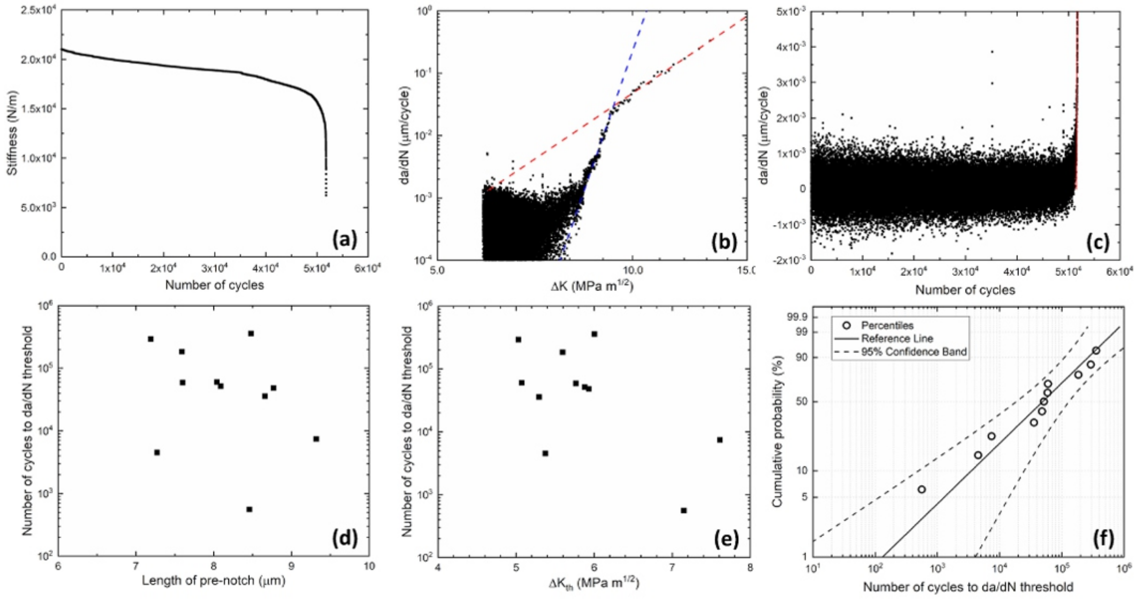

Fig. 3. Cyclic bending of IN939-Si pre-notched micro cantilevers: (a) one measurement of bending stiffness vs. number of loading cycles with the cantilever long axis oriented perpendicular to the L-PBF AM BD; (b) the corresponding da/dN - ΔK curve. The blue and red dashed lines are power law fits to the data points in the threshold and Paris-law regimes, respectively; (c) the same data shown in (a) and (b) plotted as da/dN vs. N. The red line is a linear fit to the data points near the da/ dN threshold; (d) the number of cycles to da/dN threshold (Nth) plotted vs. a o ; (e) N th plotted vs. ΔK th ; (f) a Weibull probability plot of Nth values measured from 11 separate cantilevers. The Weibull reference line and 95

% confidence bands are generated through maximum likelihood fitting. (For interpretation of the references to colour in this figure legend, the reader is referred to the Web version of this article.)

believed that using da/dN vs. N is preferable for Nth determination.

Repeat measurements were conducted on 11 separate IN939-Si micro cantilevers under the same loading conditions following the same procedures, with their pre-notches fabricated using the same Xe+ FIB milling parameters to similar pre-notch length ao. The values of so- measured Nth are plotted against ao in Fig. 3(d) and the corresponding threshold ΔK value (ΔKth) in Fig. 3(e). It is evident from Fig. 3(d) and (e) that measured Nth values vary over almost three orders of magnitude, and that correlation between Nth and either ao or ΔKth, if any, is not strong. This wide-ranging variation in Nth value is not reflected in the representation of fatigue crack growth data (Fig. 3(b)), as the da/dN vs. ΔK plots from measurements on the 11 IN939-Si cantilevers show similar shape and characteristics (ΔKth and Paris law exponent m) [27], regardless of the Nth value.

We contend that the so-determined Nth value yields a measure of the number of loading cycles needed to initiate an actual fatigue crack from the FIB milled notch, and that the variation in measured Nth values mainly reflects the variation in fatigue crack initiation under the same loading conditions and pre-notch geometry. We explored whether the widely varying Nth values measured in repeat cyclic loading experiments under nominally the same conditions would conform to two-parameter Weibull statistics [29], with a distribution function for Nth of

$$f(N_{th}) = \frac{\beta}{\delta}\left(\frac{N_{th}}{\delta}\right)^{\beta-1} exp\left[-\left(\frac{N_{th}}{\delta}\right)^{\beta}\right], \tag{3}$$

where δ >0 and β >0 are, respectively, the Weibull scale parameter and the Weibull shape parameter (Weibull modulus). The cumulative distribution function is

$$F(N_{th}) = \int_0^{N_{th}} f(t)dt = 1 - exp\left[-\left(\frac{N_{th}}{\delta}\right)^{\beta}\right], \tag{4}$$

leading to the well-known linear relationship between log of the measured Nth value and double log of the associated cumulative probability F(Nth),

$$ln[(-1)ln(1-F(N_{th}))] = \beta\, ln\left(\frac{N_{th}}{\delta}\right). \tag{5}$$

With the 11 separate measurements made on IN939-Si cantilevers, the measured Nth values were rank ordered [Nth(I), i =1, …,n, n =11; Nth(i) <Nth(i+1)], and the associated values of the cumulative probability F (Nth(I)) were estimated through the Bernard approximation for the median rank (MR(I)) of the beta distribution B (i, n+1-I) [30],

$$F(N_{th}(i)) \approx MR(i) \approx (i-0.3) / (n+0.4). \tag{6}$$

Fig. 3(e) plots the 11 data points (MR(i), Nth(i)) in a Weibull probability plot, in which the data points are shown together with the Weibull fit line and the 95 % confidence bands, obtained through maximum likelihood fitting using the Origin software (OriginPro, Version 2020, Origin lab Corporation, Northampton, MA, USA). A reasonable fit is evident in Fig. 3(e): a linear least squares fit following Eq. (5)yielded an R2 value of 0.96. This indicates that the threshold number of loading cycles to initiate an actual fatigue crack from the FIB milled notch, Nth, indeed obeys Weibull statistics under fixed loading conditions and fixed notch geometry for the IN939-Si cantilevers examined.

The results of cyclic bending of pre-notched IN939-Si micro cantilevers, summarized in Fig. 3, indicate that this test protocol is sensitive to crack initiation from a notch and can offer a quantitative measure for it. As reported previously [24], L-PBF AM IN939-Si specimens have a rather distinct microstructure, with a γ matrix decorated with dense cells of brittle Si-/Ti-/Nb-rich precipitate aligned with the AM build direction (BD) [24, 27]. It is therefore prudent to establish whether the presently described microscale testing protocol can yield a measure of Nth for fatigue crack initiation from a notch in other L-PBF AM alloys. For this reason, further measurements were performed on pre-notched microcantilevers fabricated from the L-PBF AM IN718 specimen.

Fig. 4(a) shows the XRD symmetric θ/2θ scan of the as-printed L-PBF AM IN718 disk, from which the micro cantilevers were fabricated. All the major peaks are indexed to a single FCC structure. The inset in Fig. 4 (a) shows the Nelson-Riley extrapolation [31] for the unit cell dimension of the FCC structure, which yields a lattice constant of a=3.599± 0.005 Å. The red arrow highlights a minor peak not indexed to the FCC structure. The value of the so-determined lattice constant and the presence of the minor peak not indexable to the FCC phase are both consistent with the as-printed IN718 being predominantly in the γ phase, with minor fractions of non-γ precipitates [32]. Fig. 4(b) shows a large area EBSD inverse pole figure (IPF) Z map acquired from the top surface of the same disk. Fig. 4(b) shows no strong alignment of the AM BD (Z direction) with any single crystallographic direction of the γ matrix, consistent with the presence of all major FCC reflections in Fig. 4 (a). In Fig. 4(b), the unindexed spots in the IPF Z map correspond to non-γ precipitates, dispersed sparsely and randomly in the γ matrix. The average grain size is determined to be ~27 μm from the EBSD Z map, using the boundary intersection method present within the EBSD software. It is noted that the absence of strong texture aligned with L-PBF AM BD differs from what is typically observed in as-printed specimens, and that the stress relieving heat treatment at 1066 ◦C for 90 min was the likely cause of the microstructure shown in Fig. 4.

Fig. 5(a) shows an SEM image of a typical IN718 cantilever. Both the cantilever top and front surfaces as well as the Xe+FIB milled pre-notch are evident. The inset in Fig. 5(a) is an overlay of the band contrast image of the EBSD mapping area on the cantilever top surface. Fig. 5(b) shows the same EBSD band contrast image together with the IPF X, Y, and Z maps. Fig. 5(c) shows another SEM image of the same IN718 cantilever. The inset in Fig. 5© is an overlay of the band contrast image of the EBSD mapping area on the cantilever front surface. Fig. 5(d) shows the same EBSD band contrast image together with the IPF X, Y, and Z maps. Fig. 5shows γ grain sizes consistent with what was determined from the large area EBSD map shown in Fig. 4and that there is no strong alignment of any one crystallographic direction with the AM BD (Z direction in Fig. 5(b) and Y direction in Fig. 5(d)).

ig. 6(a)–(b) show, respectively, SEM images of the top surface and front surface of the same IN718 cantilever shown in Fig. 5. The insets in Fig. 5(a)–(b) show, respectively, the EDS mapping areas on the cantilever top and front surfaces with overlays of Ni Kα, Fe Kα, Cr Kα, Nb Lα, Mo Lα intensities. EDS Ni Kα, Fe Kα, Cr Kα, Nb Lα, Mo Lα, and Ti Kα intensity maps of the cantilever top surface and front surface are shown in Fig. 6(c)–(d), respectively. It is seen that the cantilever consists of a Ni-Fe-Cr matrix with a relatively uniform composition with randomly dispersed precipitates that are rich in Nb, Mo, and Ti, consistent with data shown in Fig. 4.

The geometry of the Xe+FIB milled pre-notch in as-fabricated IN718 cantilevers prior to mechanical testing was quantified through destructive 3D tomography by “slice-and-view” performed on the PFIB/SEM instrument. Fig. 7(a) shows a low magnification SEM image taken after one “slice” of a slice-and-view experiment on one as-fabricated IN718 cantilever. The PFIB instrument uses the fiducial mark on the upper left portion of the cantilever lift-out to automatically align the ion and electron beams during successive slicing operations. A close to complete characterization of the cantilever pre-notch geometry was achieved through an extended slice-and-view operation, covering a total volume of ~15 ×~25 ×~21 μm3. The entire slice-and-view experiment can be viewed in Supplemental Information (SI) Movie 1. Fig. 7(b) shows a higher magnification image of the entire pre-notch, taken of the same slice shown in Fig. 7(a). Fig. 7(c) shows a high magnification image of the notch tip region after additional slicing operations. The same high magnification image, without and with a white circle with radius adjusted to fit that of the notch tip, is displayed in the left and right parts of Fig. 7©, respectively. This notch tip radius fitting was performed on similar high magnification images taken of the notch tip region after each slicing operation, yielding collectively an average notch tip radius

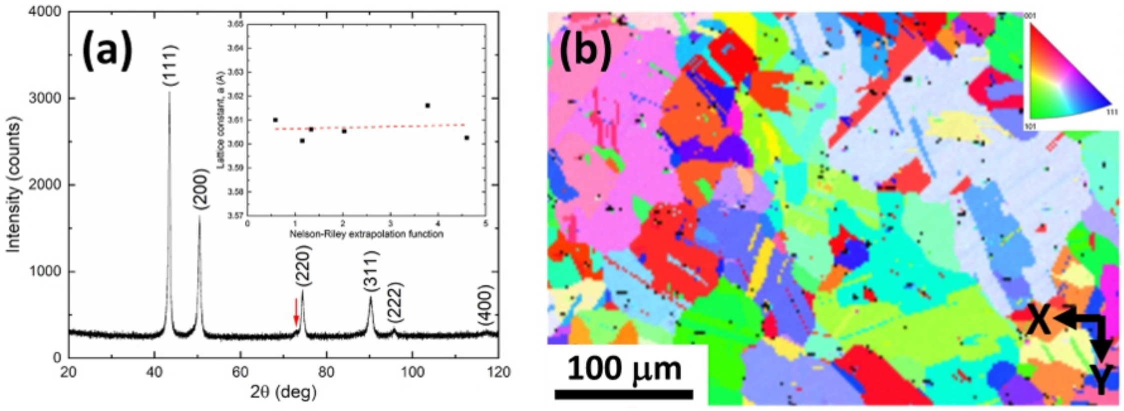

Fig. 4. Structure of as-printed IN718: (a) a symmetric θ/2θ XRD scan of the as-printed L-PBF AM IN718 disk from which the micro cantilevers are fabricated by Xe + FIB milling. The red arrow highlights a minor peak not indexed to the γ matrix; (b) a large area IPF Z map of the same specimen. (For interpretation of the references to colour in this figure legend, the reader is referred to the Web version of this article.)

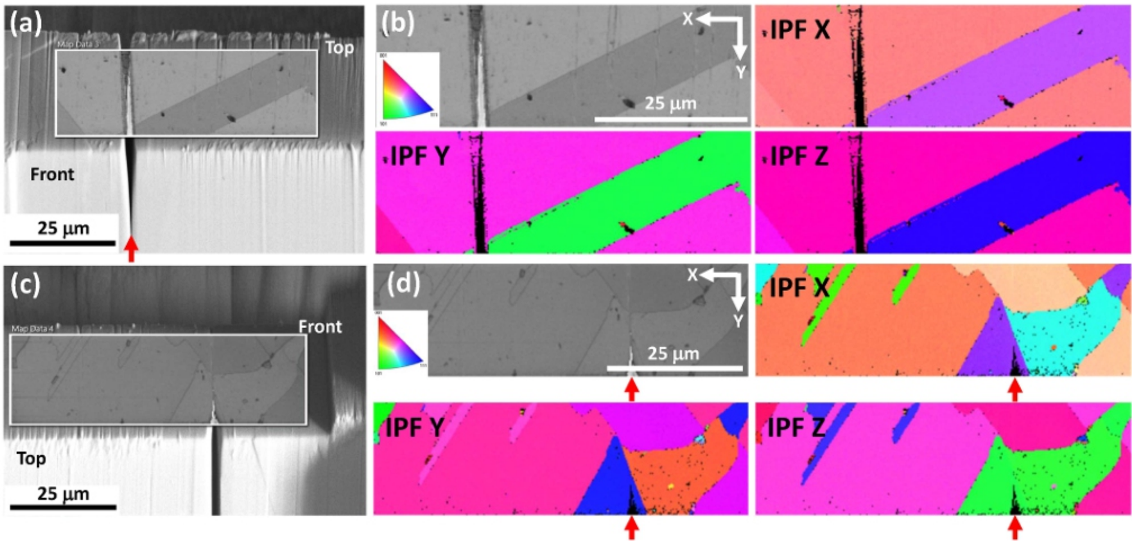

Fig. 5. Structure of IN718 pre-notched micro cantilevers: (a) an SEM image of a typical cantilever showing the top and front surfaces together with the Xe + FIB milled pre-notch, the notch tip region on the front surface is highlighted by the red arrow. The inset is the band contrast image of the EBSD mapping area on the cantilever top surface; (b) the same EBSD band contrast image shown in (a) together with the IPF X, Y, and Z maps; (c) another SEM image of the same cantilever. The inset is the band contrast image of the EBSD mapping area on the cantilever front surface; (d) the same EBSD band contrast image shown in (c) together with the IPF X, Y, and Z maps. The red arrows in (d) highlight the location of the PFIB milled pre-notch. (For interpretation of the references to colour in this figure legend, the reader is referred to the Web version of this article.)

of 5.4 ± 2.6 nm. Fig. 7(d) shows a 3D view of the Xe + FIB milled pre- notch, reconstructed from all the high magnification images taken near the notch tip region, after segmentation of empty (notch) and solid (cantilever) areas and elimination of the segmented notch area. A 3Dstacking of high magnification images taken around the Xe+FIB milled pre-notch region after each slice can be viewed in SI Movie 2. Another slice-and-view experiment performed on a separate IN718 cantilever yielded an average notch tip radius of ~7 nm, demonstrating the degree of reproducibility of the geometry of the notch tip milled under the sameXe+ FIB conditions. With the γ phase lattice constant measured at 3.599 Å, the (111) lattice spacing is ~2.1 Å or ~0.2 nm. While the pre-notches in as-fabricated cantilevers, with a sub-10 nm average tip radius, are "sharp" as compared to those in macroscale test specimens [11], they are still "blunt" from an atomistic perspective, i.e., ~30 atomic planes wide at the notch tip.

The occurrences around Xe + FIB milled pre-notches in tested cantilevers after da/dN exhibits the sharp upturn due to cyclic bending are documented in Fig. 8. Fig. 8(a) shows typical cyclic bending data for two IN718 cantilevers, plotted as da/dN vs. N. The two red lines in Fig. 8(a) are linear fits to the data points near the respective da/dN thresholds, from which N th values are obtained. It may be noticed that the extent of scatter in da/dN values in the subthreshold regime (envelope of positive and negative da/dN values shown in Fig. 8(a)) appears to decrease as N approaches N th . A similar trend may be noticed in data shown in Fig. 3 ©, albeit not as pronounced as in Fig. 8(a). This may be a reflection of an accelerating decrease of bending stiffness S as N approaches N th (see e.g., Fig. 3(a)). On top of this nascent trend, the sharp and significant upturn in da/dN when N th is reached is unmistakable. After cyclic loading, slice-and-view experiments on tested cantilevers were carried out. Fig. 8(b) shows a low magnification image taken after one slice of a

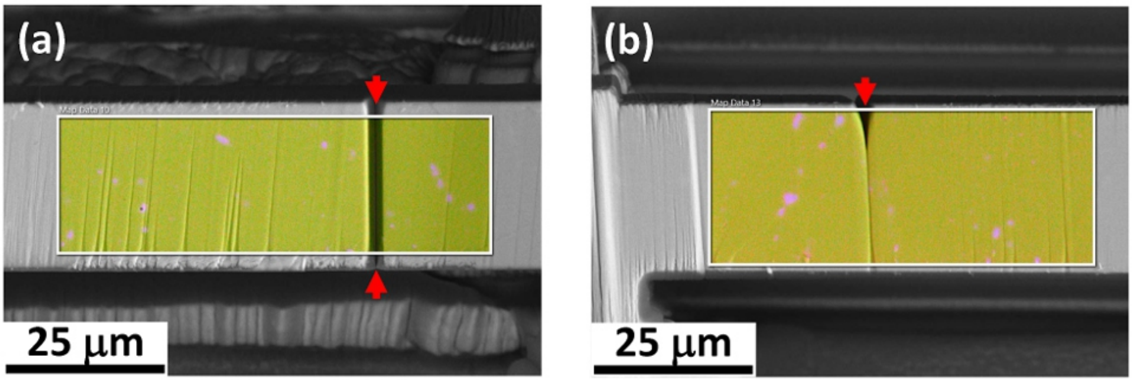

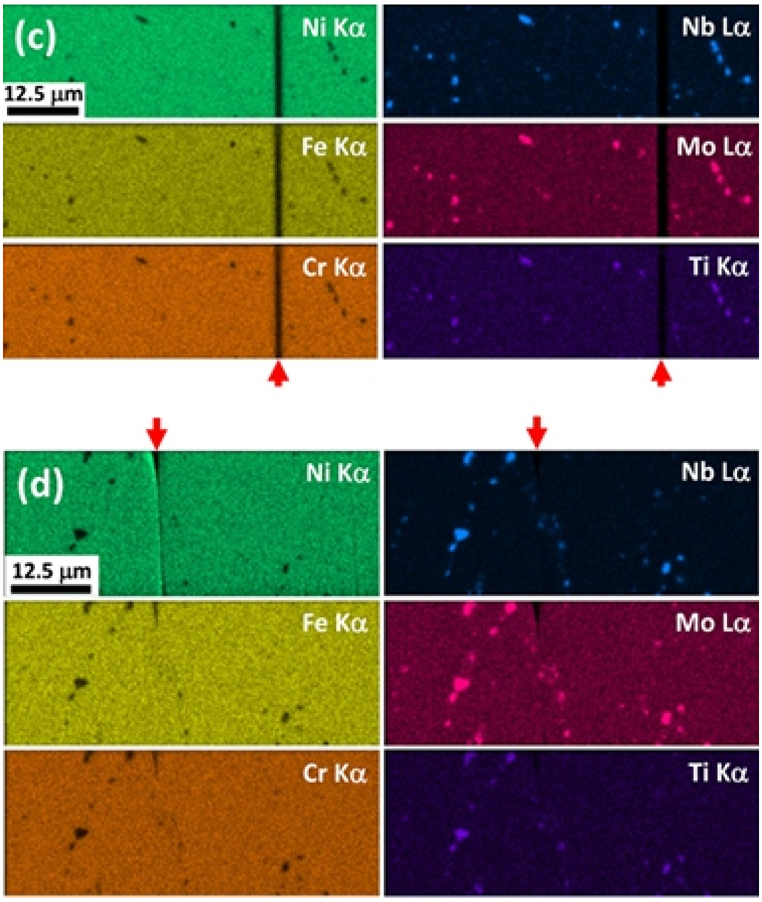

Fig. 6. Composition of IN718 pre-notched micro cantilevers: SEM images of the (a) top surface and (b) front surface of the same cantilever shown in Fig. 5. The insets in (a) and (b) show the EDS mapping areas with overlay of Ni K α , Fe K α , Cr K α , Nb L α , Mo L α intensities. EDS Ni K α , Fe Kα , Cr K α , Nb L α , Mo L α , and Ti K α intensity maps of the cantilever (c) top surface and (d) front surface. The red arrows in (a/b/c/d) highlight the location of the Xe+FIB milled pre-notch. (For interpretation of the references to colour in this figure legend, the reader is referred to the Web version of this article.)

slice-and-view experiment on one IN718 micro cantilever after test. The slice-and-view experiment can be better viewed in SI Movie 3. Fig. 8© shows a higher magnification SEM image after another slicing operation. A crack is clearly seen to emanate from the tip of the pre-notch. Fig. 8(d) shows a high magnification SEM image of the notch tip after additional slicing operations. In addition to further confirming that an actual fatigue crack emanates from the pre-notch tip, a comparison of cracks shown in Fig. 8(c)–(d) indicate that the actual fatigue crack does not stay as a flat sheet. Rather, the crack shows some meandering from slice to slice, throughout the width of the cantilever. Fig. 8(e) shows a 3D view

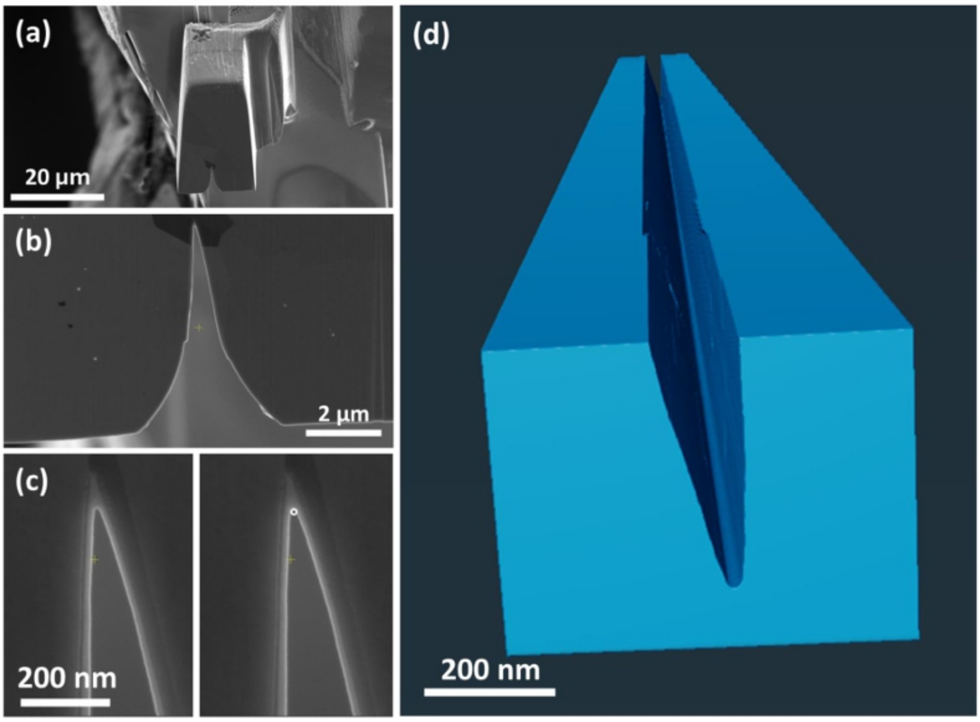

Fig. 7. Geometry of the Xe + FIB milled pre-notch: (a) a low magnification SEM image taken after one "slice" of a "slice-and-view" experiment on one as-fabricated IN718 micro cantilever; (b) a higher magnification image of the same slice; (c) a high magnification image of the notch tip region without (left) and with (right) a white circle with radius adjusted to fit that of the notch tip; (d) a 3D reconstruction by Avizo of the notch from segmentation of high magnification images taken near the notch tip at every slice.

of the cracked notch, reconstructed from high magnification images taken near the notch tip region at every slice, after segmentation of empty (notch) and solid (cantilever) areas and elimination of the segmented notch area. Data displayed in Fig. 8 show unambiguously that the actual fatigue crack emanates from the tip of the Xe+FIB milled pre-notch after cyclic bending. While FIB milled pre-notches are ~30 atomic planes wide at the notch tip (see Fig. 7), the crack morphology as observed in Fig. 8(d) shows that additional separation of neighboring atomic planes occurs when fatigue cracks form. The process of fatigue crack initiation is associated with how this additional atomic plane separation occurs from a notch that is several tens of atomic planes wide. We suggest that this process of going from a notch to a crack is associated with the observation of the sharp da/dN upturn in da/dN – N curves, as exemplified in Fig. 3(c)–8(a). The results of slice-and-view experiments, shown in Figs. 7 and 8, help to illustrate this process of fatigue crack initiation from a notch.

Repeat cyclic bending tests on pre-notched IN718 cantilevers were conducted, and Nth values were measured for each test. Fig. 9(a), 9(b), 9 (c), 9(d), and 9(e) show, respectively, Weibull probability plots for Nth measured at f = 40, 100, 400, 500, and 600 Hz, plotted following the same procedure used for the IN939-Si data shown in Fig. 3. The Weibull reference lines and 95 % confidence bands are again generated through maximum likelihood fitting. The data shown in Fig. 9 demonstrate that the number of loading cycles required to initiate an actual fatigue crackin IN718 cantilevers from Xe + FIB milled pre-notches with a fixed notch tip geometry under nominally identical loading conditions follows Weibull statistics for loading frequencies ranging from 40 Hz to 600 Hz. The fact that measured Nth values for IN718 cantilevers obey Weibull statistics at different loading frequencies provides a more solid means to quantify fatigue crack initiation. Fig. 10(a) plots ΔKth versus f for all tests performed on IN718 cantilevers and shows a relatively constant ΔKth from 40 to 600 Hz. Since all tests were conducted at relatively constant values of loads (F_{max} , F_{min}), load length (*lL*), specimen dimensions (B, t), and the depth of the pre-notch (ao), the constancy of the ΔKth valuesshown in Fig. 10(a) is thus consistent with crack initiation occurring at the tip of the pre-notch, supporting direct observations shown in Fig. 8. The average of ΔKth values shown in Figs. 10(a), 5.2 ± 0.1 MPa $m^{1/2}$, lies within the range of ΔKth values obtained for L-PBF IN718 alloys through multiple macroscale measurements, 3–15 MPa $m^{1/2}$, as summarized by Gruber et al. in Ref. 12. Fig. 10(b) plots β versus f and shows a relatively constant Weibull modulus from 40 to 600 Hz, suggesting that there are no significant shifts in crack initiation mechanism. It is noted that the Weibull scale parameter δ provides a more statistically grounded measure of the number of cycles needed to initiate a fatigue crack from a notch of fixed geometry under fixed loading conditions, with N = δ yielding a ~63 % probability for crack initiation. Fig. 10© plots δ versus f and shows a relatively constant δ value from 40 Hz to 400 Hz as well as an increasing δ value as f increases further from 400 Hz to 600Hz, from slightly less than 200,000 cycles at 40 Hz and 400 Hz to slightly more than 300,000 cycles at 600 Hz. The present observation of Nth increasing with increasing loading frequency is qualitatively consistent with previous observations of increasing total fatigue life and fatigue strength as loading frequency increases from <100 Hz to 20 kHz [8, 21]. The results summarized in Figs. 3, 8 and 9 indicate that cyclic

bending of pre-notched micro cantilevers is indeed sensitive to initiation of a fatigue crack from a FIB milled sharp notch for both IN939-Si and IN718, two alloys having rather different microstructural characteristics. It is thus surmised that the present microscale testing protocol can be used to gauge fatigue crack initiation quantitatively in a wide range of alloys. The present measurements also show that N th obeys Weibull

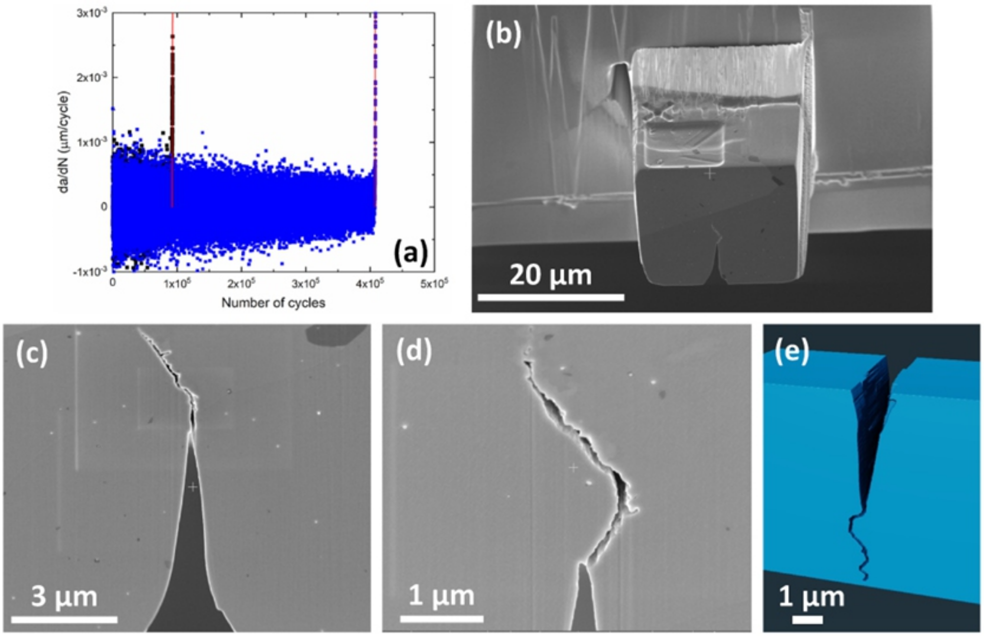

Fig. 8. Crack initiation from Xe + FIB milled pre-notches: (a) cyclic bending data for two cantilevers (data points shown in black and blue) plotted as da/dN vs. N. The two red lines are linear fits to the data points near the da/dN threshold; (b) a low magnification image taken after one "slice" of a "slice-and-view" experiment on one IN718 micro cantilever after test; (c) an image after another slice of the notch tip from which the fatigue crack emanates; (d) a high magnification image after another slice of the notch tip region; (e) a 3D view of the cracked notch reconstructed by Avizo from high magnification images taken near the notch tip at every slice after segmentation. (For interpretation of the references to colour in this figure legend, the reader is referred to the Web version of this article.)

statistics for both IN939-Si and IN718, despite the significant differences in their microstructure.

Fatigue crack initiation from a notch, the process of generating additional atomic plane separation from the tip of a notch that is sharp on a macroscopic scale yet blunt from an atomistic perspective, is a consequence of dislocation motion under cyclic stresses [33]. Mura and Nakasone have discussed the process of fatigue crack initiation through a vacancy – dislocation dipole model of persistent slip band [34]. They listed several variables that can influence the S-N curve for crack initiation, including frictional stress, Young's modulus, surface energy, half-length of the persistent slip band, and height of the dislocationdipole [34]. For the present experiments on IN718, variations in frictional stress and Young's modulus can be eliminated from consideration as the predominant γ matrix remained a constant factor throughout. Intrinsic variabilities exist in the present experiments, as the cantilevers and pre-notches were fabricated at random locations on the IN718 alloy disk, which leads to variations in the local environment around the notch tip.Nonetheless, the variation in surface energy is not expected to be significant. While no attempts were made to observe the presence and quantify the geometry of persistent slip bands, the question remains whether variations in persistent slip band geometry (e.g., band length and dislocation dipole height) can account for the observed two to three orders of magnitude variation in observed Nth values (cf. Figs. 3 and 9). Moreover, it is unclear why the combined variation in such parameters would result in observed Nth values obeying Weibull statistics. Answering these questions necessitates additional experimentation and modeling in the future, included in which is a better understanding of the effects of loading frequency on crack initiation from sharp notches.

4. Summary

The present results of cyclic bending of pre-notched micro cantilevers fabricated from L-PBF AM IN939-Si and IN718 specimens indicate that this test protocol is sensitive to fatigue crack initiation from a nm- scaled sharp notch and can provide a quantitative measure for the threshold number of cycles needed for crack initiation. Repeat measurements performed under the same loading conditions and the same notch geometry on both IN939-Si and IN718 cantilevers indicate that measured Nth values from repeat tests obey Weibull statistics, which in turn provides a more statistically grounded measure for fatigue crack initiation from a notch. Measurements on IN718 cantilevers indicate a relatively constant Nth increase in Nth in the frequency range of 40–400 Hz and a modest as the loading frequency increases from 400 Hz to 600 Hz. Better quantitative gauging of the crack initiation process may lead to improved understanding and more effective means for controlling fatigue damage and life of materials, inclusive of materials fabricated by L- PBF AM processes.

CRediT authorship contribution statement

Ali Kaveh: Methodology, Investigation, Formal analysis, Data curation. **M.H. Shahini:** Methodology, Investigation, Formal analysis, Data curation. **Xiaoman Zhang:** Writing – original draft, Methodology, Investigation, Formal analysis, Data curation. **Wangwang Xu:** Writing – original draft, Software, Methodology, Investigation. **Parisa Z. Firouzabadi:** Methodology, Investigation, Formal analysis, Data curation. **Bin Zhang:** Writing – original draft, Methodology, Investigation, Formal

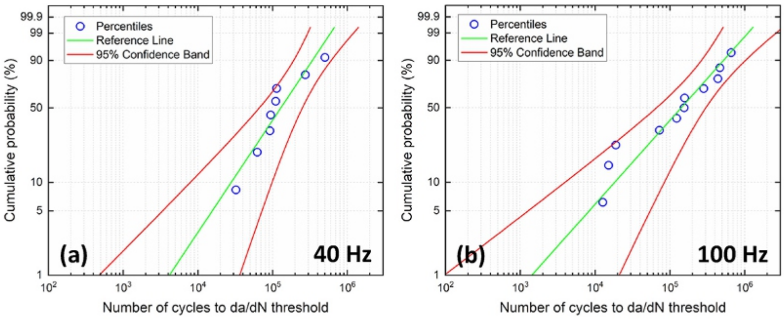

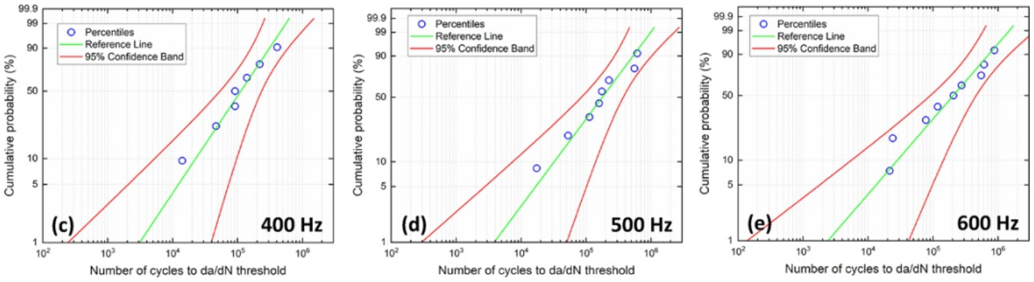

Fig. 9. Nth values for IN718 pre-notched micro cantilevers measured at different loading frequencies: Weibull probability plots of N values at f of (a) 40 Hz, (b) 100 Hz, (c) 400 Hz, (d) 500 Hz, (e) 600 Hz. The Weibull reference lines and 95 % confidence bands are generated through maximum likelihood fitting.

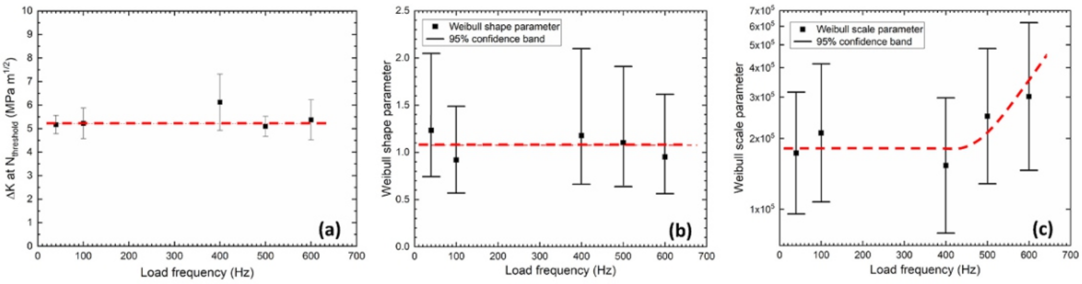

Fig. 10. Result of cyclic bending tests on IN718 pre-notched micro cantilevers: (a) value of the threshold stress intensity factor range ΔKth plotted versus the load frequency; (b) Weibull shape parameter and (c) Weibull scale parameter obtained from Weibull fits to Nth values measured through multiple tests plotted versus the load frequency. The red dashed lines in (a/b/c) are guides to the eye. (For interpretation of the references to colour in this figure legend, the reader is referred to the Web version of this article.)

analysis, Data curation. **W.J. Meng:** Writing – review & editing, Writing – original draft, Supervision, Project administration, Methodology, Investigation, Funding acquisition, Formal analysis, Data curation, Conceptualization.

Data statement

Data associated with this study will be made available upon reasonable request.

Declaration of competing interest

The authors declare that they have no known competing financial interests or personal relationships that could have appeared to influence the work reported in this paper.

Acknowledgements

This work was funded in part by the NSF EPSCoR program under awards OIA-2118756 and OIA-1946231, and the Louisiana Board of Regents. The use of experimental facilities at the LSU Shared Instrumentation Facility (SIF), a part of the Louisiana Core User Facilities (CUF), is acknowledged. WJM acknowledges ACM for helpful discussions and Prof. J.W. Hutchinson for a reading of the manuscript.

Appendix A. Supplementary data

Supplementary data to this article can be found online at https://doi. org/10.1016/j.msea.2025.148187.

Data availability

Data will be made available on request.

References

[1] E. Epremian, R.F. Mehl, Investigation of Statistical Nature of Fatigue Properties, National Advisory Committee for Aeronautics Technical Note 2719 (NACA-TN- 2719), June 1952.

[2] R. Sakin, I. Ay, Statistical analysis of bending fatigue life data using Weibull distribution in glass-fiber reinforced polyester composites, Mater. Des. 29 (2008) 1170–1181.

[3] S. Shimizu, H. Shimoda, K. Tosha, Study on the life distribution and reliability of roller-based linear bearing, Tribol. Trans. 51 (2008) 446–453.

[4] S. Shimizu, K. Tsuchiya, K. Tosha, Probabilistic stress-life (P-S-N) study on bearing steel using alternating torsion life test, Tribol. Trans. 52 (2009) 807–816.

[5] Q.G. Wang, D. Apelian, D.A. Lados, Fatigue behavior of A356-T6 aluminum cast alloys. Part I. Effect of casting defects, J. Light Met. 1 (2001) 73–84.

[6] W. Schutz, The prediction of fatigue life in the crack initiation and propagation stages – a state of the art survey, Eng. Fract. Mech. 11 (1979) 405–421.

[7] J. Schijve, Fatigue of structures and materials in the 20th century and the state of the art, Int. J. Fatig. 25 (2003) 679–702.

[8] X. Zhu, J.W. Jones, J.E. Allison, Effect of frequency, environment, and temperature on fatigue behavior of E319 cast aluminum alloy: stress-controlled fatigue life response, Metall. Mater. Trans. A 39A (2008) 2681–2688.

[9] A. Yadollahi, N. Shamsaei, Additive manufacturing of fatigue resistant materials: challenges and opportunities, Int. J. Fatig. 98 (2017) 14–31.

[10] B. Zhang, W.J. Meng, S. Shao, N. Phan, N. Shamsaei, Effect of heat treatments on pore morphology and microstructure of laser additive manufactured parts, Mater. Des. Proc. Commun. 1 (2019) e29/1–8.

[11] ASTM E647 - 23, Standard Test Method for Measurement of Fatigue Crack Growth Rates, ASTM International, 2023.

[12] K. Gruber, P. Szymczyk-Ziolkowski, S. Dziuba, S. Duda, Pawel Zielonka, S. Seitl, G. Lesiuk, Fatigue crack growth characterization of Inconel 718 after additive manufacturing by laser powder bed fusion and heat treatment, Int. J. Fatig. 166 (2023) 107287/1–10728713.

[13] ASTM E466 - 15, Standard Practice for Conducting Force Controlled Constant Amplitude Axial Fatigue Tests of Metallic Materials, ASTM International, 2015.

[14] P. Li, D.H. Warner, A. Fatemi, N. Phan, Critical assessment of the fatigue performance of additively manufactured Ti–6Al–4V and perspective for future research, Int. J. Fatig. 85 (2016) 130–143.

[15] S. Romano, A. Brückner-Foit, A. Brand˜ ao, J. Gumpinger, T. Ghidini, S. Beretta, Fatigue properties of AlSi10Mg obtained by additive manufacturing: defect-based modelling and prediction of fatigue strength, Eng. Fract. Mech. 187 (2018)
165–189.

[16] K.S. Chan, M. Koike, R.L. Mason, T. Okabe, Fatigue life of titanium alloys fabricated by additive layer manufacturing techniques for dental implants, Metall. Mater. Trans. A 44A (2013) 1010–1022.

[17] S. Beretta, S. Romano, A comparison of fatigue strength sensitivity to defects for materials manufactured by AM or traditional processes, Int. J. Fatig. 94 (2017) 178–191.

[18] T. Nicholas, High Cycle Fatigue, A Mechanics of Materials Perspective, Elsevier, Amsterdam, 2006.

[19] H. Mayer, Recent developments in ultrasonic fatigue, Fatigue Fract, Engng. Mater. Struct. 39 (2016) 3–29.

[20] J. Schijve, Fatigue of Structures and Materials, second ed., Springer Dordrecht, 2009.

[21] R.J. Morrissey, D.L. McDowell, T. Nicholas, Frequency and stress ratio effects in high cycle fatigue of Ti–6Al–4V, Int. J. Fatig. 21 (1999) 679–685.

[22] H. Wen, Laser surface treatment and laser powder bed fusion additive manufacturing study using custom designed 3D printer and the application of machine learning in materials science, LSU Doctoral Dissertations #5640, https://r epository.lsu.edu/gradschool_dissertations/5640, 2021.

[23] H. Wen, C. Zeng, A.H. Ettefagh, J. Gao, S. Guo, Laser surface treatment of Ti-10Mo alloy under Ar and N2 environment for biomedical application, J. Laser Appl. 31 (2019), 022012/1-9.

[24] B. Zhang, H. Ding, A.C. Meng, S. Nemati, S. Guo, W.J. Meng, Crack reduction in Inconel 939 with Si addition processed by laser powder bed fusion additive manufacturing, Addit. Manuf. 72 (2023) 103623/1–10362315.

[25] ISO/ASTM 52901:2017(E), Additive Manufacturing — General Principles — Requirements for Purchased AM Parts, ISO/ASTM International, 2017.

[26] P.R. Gradl, D.C. Tinker, J. Ivester, S.W. Skinner, T. Teasley, J.L. Bili, Geometric feature reproducibility for laser powder bed fusion (L-PBF) additive manufacturing with Inconel 718, Addit. Manuf. 47 (2021) 102305/1–10230533.

[27] M.H. Shahini, A. Kaveh, B. Zhang, H. Ghadimi, S. Guo, C. Zeng, W.J. Meng, Measuring fatigue crack growth using microscale specimens: Si-modified Inconel 939 alloy processed by laser powder bed fusion additive manufacturing, Mater. Sci. Eng., A 913 (2024) 147032/1–14703212.

[28] F. Iqbal, J. Ast, M. Goken, K. Durst, In situ micro-cantilever tests to study fracture properties of NiAl single crystals, Acta Mater. 60 (2012) 1193–1200.

[29] D.C. Montgomery, G.C. Runger, Applied Statistics and Probability for Engineers, Wiley, New York, 2003.

[30] B.C. Arnold, N. Balakrishnan, H.N. Nagaraja, A First Course in Order Statistics, Wiley, New York, 1992.

[31] J.B. Nelson, D.P. Riley, An experimental investigation of extrapolation methods in the derivation of accurate unit-cell dimensions of crystals, Proc. Phys. Soc. 57 (1945) 160–177.

[32] W.C. Liu, F.R. Xiao, M. Yao, Z.L. Chen, Z.Q. Jiang, S.G. Wang, Relationship between the lattice constant of γ phase and the content of δ phase, γ" and γ' phases in Inconel 718, Scripta Mater. 37 (1) (1997) 59–64.

[33] S. Suresh, Fatigue of Materials, second ed., Cambridge University Press, Cambridge, UK, 1998.

[34] T. Mura, Y. Nakasone, A theory of fatigue crack initiation in solids, J. Appl. Mech. 57 (1990) 1–6.

Instructions for Authors

Essentials for Publishing in this Journal

1 Submitted articles should not have been previously published or be currently under consideration for publication elsewhere.

2 Conference papers may only be submitted if the paper has been completely re-written (taken to mean more than 50%) and the author has cleared any necessary permission with the copyright owner if it has been previously copyrighted.

3 All our articles are refereed through a double-blind process.

4 All authors must declare they have read and agreed to the content of the submitted article and must sign a declaration correspond to the originality of the article.

Submission Process

All articles for this journal must be submitted using our online submissions system. http://enrichedpub.com/ . Please use the Submit Your Article link in the Author Service area.

Manuscript Guidelines

The instructions to authors about the article preparation for publication in the Manuscripts are submitted online, through the e-Ur (Electronic editing) system, developed by **Enriched Publications Pvt. Ltd**. The article should contain the abstract with keywords, introduction, body, conclusion, references and the summary in English language (without heading and subheading enumeration). The article length should not exceed 16 pages of A4 paper format.

Title

The title should be informative. It is in both Journal's and author's best interest to use terms suitable. For indexing and word search. If there are no such terms in the title, the author is strongly advised to add a subtitle. The title should be given in English as well. The titles precede the abstract and the summary in an appropriate language.

Letterhead Title

The letterhead title is given at a top of each page for easier identification of article copies in an Electronic form in particular. It contains the author's surname and first name initial .article title, journal title and collation (year, volume, and issue, first and last page). The journal and article titles can be given in a shortened form.

Author's Name

Full name(s) of author(s) should be used. It is advisable to give the middle initial. Names are given in their original form.

Contact Details

The postal address or the e-mail address of the author (usually of the first one if there are more Authors) is given in the footnote at the bottom of the first page.

Type of Articles

Classification of articles is a duty of the editorial staff and is of special importance. Referees and the members of the editorial staff, or section editors, can propose a category, but the editor-in-chief has the sole responsibility for their classification. Journal articles are classified as follows:

Scientific articles:

1. Original scientific paper (giving the previously unpublished results of the author's own research based on management methods).
2. Survey paper (giving an original, detailed and critical view of a research problem or an area to which the author has made a contribution visible through his self-citation);
3. Short or preliminary communication (original management paper of full format but of a smaller extent or of a preliminary character);
4. Scientific critique or forum (discussion on a particular scientific topic, based exclusively on management argumentation) and commentaries. Exceptionally, in particular areas, a scientific paper in the Journal can be in a form of a monograph or a critical edition of scientific data (historical, archival, lexicographic, bibliographic, data survey, etc.) which were unknown or hardly accessible for scientific research.

Professional articles:

1. Professional paper (contribution offering experience useful for improvement of professional practice but not necessarily based on scientific methods);
2. Informative contribution (editorial, commentary, etc.);
3. Review (of a book, software, case study, scientific event, etc.)

Language

The article should be in English. The grammar and style of the article should be of good quality. The systematized text should be without abbreviations (except standard ones). All measurements must be in SI units. The sequence of formulae is denoted in Arabic numerals in parentheses on the right-hand side.

Abstract and Summary

An abstract is a concise informative presentation of the article content for fast and accurate Evaluation of its relevance. It is both in the Editorial Office's and the author's best interest for an abstract to contain terms often used for indexing and article search. The abstract describes the purpose of the study and the methods, outlines the findings and state the conclusions. A 100- to 250-Word abstract should be placed between the title and the keywords with the body text to follow. Besides an abstract are advised to have a summary in English, at the end of the article, after the Reference list. The summary should be structured and long up to 1/10 of the article length (it is more extensive than the abstract).

Keywords

Keywords are terms or phrases showing adequately the article content for indexing and search purposes. They should be allocated heaving in mind widely accepted international sources (index, dictionary or thesaurus), such as the Web of Science keyword list for science in general. The higher their usage frequency is the better. Up to 10 keywords immediately follow the abstract and the summary, in respective languages.

Acknowledgements

The name and the number of the project or programmed within which the article was realized is given in a separate note at the bottom of the first page together with the name of the institution which financially supported the project or programmed.

Tables and Illustrations

All the captions should be in the original language as well as in English, together with the texts in illustrations if possible. Tables are typed in the same style as the text and are denoted by numerals at the top. Photographs and drawings, placed appropriately in the text, should be clear, precise and suitable for reproduction. Drawings should be created in Word or Corel.

Citation in the Text

Citation in the text must be uniform. When citing references in the text, use the reference number set in square brackets from the Reference list at the end of the article.

Footnotes

Footnotes are given at the bottom of the page with the text they refer to. They can contain less relevant details, additional explanations or used sources (e.g. scientific material, manuals). They cannot replace the cited literature.

The article should be accompanied with a cover letter with the information about the author(s): surname, middle initial, first name, and citizen personal number, rank, title, e-mail address, and affiliation address, home address including municipality, phone number in the office and at home (or a mobile phone number). The cover letter should state the type of the article and tell which illustrations are original and which are not.

Note